

CROSSTALK AND COUPLING IN REFLECTOMETRY TESTING OF ELECTRICAL WIRE FAULTS

by

Lucas R. Thomson

A thesis submitted to the faculty of
The University of Utah
in partial fulfillment of the requirements for the degree of

Master of Science

Department of Electrical and Computer Engineering

The University of Utah

May 2015

Copyright © Lucas R. Thomson 2015

All Rights Reserved

The University of Utah Graduate School

STATEMENT OF THESIS APPROVAL

The thesis of Lucas R. Thomson

has been approved by the following supervisory committee members:

<u>Cynthia Furse</u>	, Chair	<u>3/21/2014</u> <small>Date Approved</small>
----------------------	---------	--

<u>Behrouz Farhang</u>	, Member	<u>3/21/2014</u> <small>Date Approved</small>
------------------------	----------	--

<u>Faisal Khan</u>	, Member	<u>3/26/2014</u> <small>Date Approved</small>
--------------------	----------	--

and by Gianluca Lazzi, Chair/Dean of

the Department/College/School of Electrical and Computer Engineering

and by David B. Kieda, Dean of The Graduate School.

ABSTRACT

The focus of this thesis is the impact and use of crosstalk and coupling when testing for electrical wiring faults using reflectometry. This thesis describes a method for detecting and locating faults on cable shields using an adapted reflectometry system. A signal transmitted on the inner conductor is coupled to the outside through the fault, a small aperture in the cable shielding. This very small signal is then detected and correlated with the original signal transmitted on the inner conductor. The signals that leak out of the aperture, the damaged shield, and propagate down the outside of the cable are quantified as a function of the aperture size and frequency. A ferrite loaded toroidal sensor design is also proposed for receiving this external signal in order to both detect and localize the shield damage. Both simulations and measurements validate the effectiveness of this method.

Unshielded discrete wires are another common type of transmission line. While unshielded wires are primarily used for DC power, they are still subject to degradation over time and require maintenance. Unlike shielded cables, there is a significant amount of coupling that occurs between adjacent wires during a reflectometry test. This coupling is quantified and evaluated for two applications. The first is simultaneous testing of multiple adjacent wires in a bundle. In this case, minimizing the coupling is desirable in order to reduce noise in the reflectometry signature. The second is the exploration of the potential for a single reflectometry test to locate faults on adjacent wires without directly testing them. When a single test is performed in a multiwire bundle, the reflectometry signature will be a superposition of reflections from all nearby conductors. This thesis addresses the testing of a multiconductor wiring structure with a common signal reference as well as a similar structure with an isolated signal reference. In order to accurately detect faults on multiconductor wiring structures, both testing methods must be considered. A fault between a conductor and its reference conductor is easily detectable. A cross fault between two nonreference conductors is not. For cross fault consideration, the only method for detection is using a common signal reference and analyzing the data on adjacent lines.

CONTENTS

ABSTRACT	iii
LIST OF FIGURES	vi
LIST OF TABLES	viii
 CHAPTERS	
1. INTRODUCTION	1
1.1 The Wiring Problem	1
1.2 Contributions of This Work	2
2. BACKGROUND	4
2.1 Coupling	4
2.1.1 Coupling Through a Shield Aperture	5
2.1.2 Coupling of Discrete Pairs in Wiring Bundles	6
2.2 S/SSTDOR	7
2.2.1 Correlation Methods	11
2.3 Simulation Methods	12
2.3.1 Modeling Shield Apertures	12
2.3.2 Modeling Discrete Wiring Structures	12
2.4 Proposed Method of Fault Location	14
3. LOCATING SMALL APERTURES IN CABLE SHIELDING	15
3.1 Fields Leaking from a Shield Aperture	15
3.2 External Propagation	19
3.3 Sensor Characterization	22
3.3.1 Windings	23
3.3.2 Wire Gauge	24
3.3.3 Geometry	24
3.3.4 Materials	25
3.3.5 Sensor Specifications	26
3.4 Aperture Localization	27
4. COUPLING CROSSTALK IN MULTICONDUCTOR WIRING STRUCTURES	31
4.1 Simulation Methods	33
4.1.1 Finite Difference Time Domain (FDTD) for Coupled Lines	33
4.1.2 Finite Difference Method (FDM) Modeling	37
4.1.3 Simulation Validation	41
4.2 Coupling Crosstalk	41

4.2.1 Isolated Reference Testing	43
4.3 Analysis Methods	45
4.3.1 Time Domain Derivatives	46
4.3.2 Standard Deviation of Noise Floor	47
4.4 Results.....	49
4.4.1 Common Reference Configuration	49
4.4.2 Isolated Reference Configuration	53
5. CONCLUSION	57
5.1 Summary of Aperture Coupling	57
5.2 Summary of Wire to Wire Coupling	58
5.3 Final Thoughts	58
REFERENCES	60

LIST OF FIGURES

2.1	Correlation coefficient vs. wiring pair separation distance	8
2.2	STDR vs. SSTDR correlation waveform	9
2.3	Maximal Length PN code generator	9
2.4	Circular correlation of a 7-bit Maximal Length PN code	10
2.5	Maximal Length PN code length comparison with Gaussian noise	10
2.6	Circular correlation vs. zero padding correlation	11
2.7	Small aperture in a coaxial transmission line	14
3.1	Magnetic field leaking from a coaxial aperture	16
3.2	Magnetic sensor for aperture localization	16
3.3	Aperture effects on a Gaussian pulse vs. propagation distance	17
3.4	Aperture response for various widths	18
3.5	Aperture response for various lengths	19
3.6	VOP for external RG58 propagation	20
3.7	Calculated RLGC parameters for external RG58 propagation	21
3.8	Sensor step response with varied windings	23
3.9	Sensor step response of a ferrite for various cross-sectional areas	25
3.10	Sensor step response of a ferrite for various radii	26
3.11	Sensor time domain step response of various ferrite materials	27
3.12	Measure frequency response of an aperture	28
3.13	Localization of various 5mm apertures	29
3.14	Localization of various 15mm apertures	29
4.1	3-wire multiconductor transmission line circuit schematic	35
4.2	Multiconductor common reference configuration	38
4.3	Electric field for a common reference multiconductor configuration	38
4.4	FDM multiconductor setup	40
4.5	Measured and simulated voltage comparison	42
4.6	Multiconductor isolated reference configuration	44
4.7	Short circuit, open circuit, and matched termination STDR waveforms	46

4.8 First and second derivative of STDR correlation	47
4.9 Common reference simulation result	48
4.10 Common reference aggressor to reference wire fault	50
4.11 Common reference victim to reference wire fault	51
4.12 Common reference aggressor to victim wire fault	52
4.13 Common reference victim to victim wire fault	53
4.14 Isolated reference aggressor to reference wire fault	55
4.15 Isolated reference aggressor to victim wire fault	56

LIST OF TABLES

3.1	Extracted RLGC parameters	22
4.1	Simulation parameters for 4-wire ribbon cable in Figure 4.4	40
4.2	Inductance matrix of the 4-wire ribbon cable in Figure 4.4	40
4.3	Capacitance matrix of the 4-wire ribbon cable in Figure 4.4	40

CHAPTER 1

INTRODUCTION

Despite the large move to optical and wireless systems in recent years, the majority of today's modern electronic systems still rely on old-fashioned conductor transmission lines. Over time, these lines age, decay, and fray, which will affect the performance and safety of the systems they support. Locating these wiring faults is an increasing problem in many industries today with the age of most wiring systems exceeding their expected lifetime [1]. Aging aircraft wiring is an area of critical national concern [1]. Electrical faults on large, vibrating vehicles and machinery, such as an aircraft, are often intermittent. Problems occur in flight and often disappear before the plane lands, creating the frustrating maintenance challenge of No Fault Found (NFF) [2]. In order to find these intermittent faults, sequence (STDR) or spread spectrum time domain reflectometry (SSTDR) has been developed [2]. These methods send a high frequency pseudo noise (PN) code down the wire, where it reflects off of impedance discontinuities, including the fault, and returns to the test point. The incident and reflected signals are correlated using an analog correlator, which provides an S/SSTDR reflectometry signature that is similar in nature to a pulsed TDR signature and can be evaluated in much the same way. The time delay between the incident and reflected signals (multiplied by the velocity of propagation (VOP)) tells the distance to the fault. The magnitude and polarity (positive/negative) of the reflection tells the value and nature of the fault.

1.1 The Wiring Problem

Reflectometry is a tested method for locating hard faults in wiring structures that works on a large variety of transmission lines and even live wires [1][2][3]. A soft fault occurs when a transmission line is damaged but still operational, such as an aperture in coaxial shielding. Traditional reflectometry methods are not sufficient for detecting such faults as the reflection is often too short in duration and smaller in magnitude than the noise within the system [4]. These types of soft faults comprise a considerable amount of the faults observed in

wiring structures [5]. New methods for detecting soft faults, such as shield apertures, are necessary.

Coaxial cables are shielded against environmental noise, and since their geometry is fixed, they are a controlled impedance transmission line. Unlike coaxial cables, discrete wires are not controlled impedance and that impedance can vary from vibrations and other physical stresses [4]. They are also subject to environmental noise, including coupling crosstalk from adjacent wires, which can corrupt any existing signal on the line [7][8][9]. When these lines degrade and breakdown, maintenance becomes necessary. Using a discrete wire and a reference conductor, reflectometry can be used to diagnose these wiring faults [1][2][6][4][10]. S/SSTDR is a relatively new method of reflectometry that is less susceptible to this type of environmental noise unlike traditional methods such as time domain reflectometry (TDR) and frequency domain reflectometry (FDR) [2][10]. During reflectometry testing in the proximity of multiple wires, the transmission lines are still subject to coupling crosstalk and the signal can become corrupted. S/SSTDR signals have a very low correlation value with other signals; however, the correlation value with other S/SSTDR signals is significant. A detailed analysis on this type of coupling crosstalk in reflectometry is not currently available. If two or more transmission lines are each carrying a similar reflectometry signal and this coupling crosstalk occurs, these reflectometry signals can become corrupted and interfere with the ability to accurately locate a wiring fault. This thesis will address such crosstalk in the application of S/SSTDR fault detection on unshielded discrete wiring bundles.

1.2 Contributions of This Work

The contributions of this thesis are a novel approach for locating coaxial cable shield apertures and an analysis of coupling crosstalk on unshielded discrete wire transmission lines, specifically pertaining to S/SSTDR testing. This thesis will address a new method for locating small apertures in coaxial cable shielding by means of a ferrite loaded toroidal sensor. This will include characterization of the frequency response of coaxial apertures as well as an analysis of the characteristic of a toroidal sensor. This work will also address coupling crosstalk in S/SSTDR for two separate configurations: 1) using a central ground plane as a common reference for multiconductor bundles and 2) simultaneous testing of two or more wiring pairs without a common reference. The goal of this analysis is to determine the effects of crosstalk coupling in S/SSTDR waveforms. This thesis is organized into the following sections.

- The following chapter, Chapter 2, will provide background information on the different

types of coupling pertinent to this work: aperture coupling and transmission line to transmission line coupling. S/SSTDR waveforms and methods are also discussed. FDM and FDTD simulation methods will also be summarized to explain the application of calculating the transmission line to transmission line coupling as well as the crosstalk from one line to another. A more in depth explanation of the methodology is detailed in Chapter 4.

- Chapter 3 will discuss the method of localizing small shield apertures. This will include an analysis of the apertures and their frequency response. A sensor design and characterization are also included for the use of localizing the apertures. This will conclude with the localization of several small apertures in a section of RG58 coaxial cable using the proposed sensor.
- Chapter 4 details the numerical methods used to obtain the crosstalk coupling parameters as well as the method for simulating multiconductor transmission lines with S/SSTDR. A Finite Difference Method simulation was used in calculating the coupling between discrete unshielded wires. After the coupling parameters were calculated, a Finite Difference Time domain algorithm was then implemented to calculate the amount of crosstalk on adjacent wires subject to electromagnetic coupling. Two reference configurations are discussed: using a common reference, such as the use of an airframe or a single reference conductor within a bundle, and testing multiconductor bundles without using a common reference between pairs.
- The final chapter will summarize the results of the entire works performed and include final thoughts on this research topic.

CHAPTER 2

BACKGROUND

The objective of this thesis is to analyze coupling in reflectometry applications, specifically with shield apertures and crosstalk between conductors due to electromagnetic coupling. The first section of this chapter will focus on coupling in general and move into the specific types of coupling to this thesis (Section 2.1). The coupling is necessary to understanding how signals are affected as they move through an aperture, or are coupled from one transmission line to another. When this coupling occurs, the signal undergoes filtering effects that will affect the spectra of the signal. This can degrade the fidelity of the signal used in the system under test. Section 2.2 will discuss S/SSTD, how to create the PN codes, and the difference between STD and SSTD. The correlation method used for analyzing the S/SSTD waveforms will also be discussed. It is important to understand how S/SSTD waveforms behave in terms of filtering, as well as how to interpret the waveforms. A mistake in waveform interpretation can lead to assigning a fault location to a false peak in the waveform where no fault is present. Section 2.3 will provide the background information on the simulation methods used in this thesis. In order to calculate the coupling parameters, accurate numerical methods are required for performing the simulations. Time domain effects must also be considered when crosstalk occurs since high frequency signals couple very differently from low frequency signals. The final section of this chapter (Section 2.4) will summarize the proposed method for locating shield apertures and testing multiconductor wiring bundles while accounting for crosstalk coupling using S/SSTD.

2.1 Coupling

Electromagnetic coupling occurs when power is transferred from one structure to another. While this transfer of power can occur intentionally, it is often undesired as the power from the coupled signal (the aggressor) gets superimposed onto the existing signal (the victim). The victim transmission line signal is now corrupted by the aggressor. There are two types of coupling that will be examined: the coupling of a signal from one transmission

line to another through a small aperture, and transmission line to transmission line type coupling via mutual inductance and mutual capacitance.

2.1.1 Coupling Through a Shield Aperture

Locating faults in shielded cables is a difficult task. Cables are shielded to protect their sensitive signals from external noise or to prevent their signals from leaking out into the environment. A fault in the shield generally has minimal impact on the ability of the cable to carry the desired signal, but rather its ability to shield or be shielded from noise. As such, cable shield faults often show up only intermittently and to varying degrees in the electrical and diagnostic systems.

This thesis presents a new method for detecting and locating damaged cable shields. The proposed method, while being based upon reflectometry, is slightly different. Reflectometry is a very effective technique for finding faults on a cable by sending a high frequency signal down the line and receiving reflections off of impedance changes such as those caused by wiring faults. The distance to the fault is found from the time delay between the incident and the reflected signals. The nature of the fault is found from the polarity (positive/negative) of the returned signal and its magnitude. The magnitude of the reflection is controlled by the size of the fault. Large faults (often called hard faults) such as open and short circuits return a reflection of ± 1 times the incident signal magnitude. Small faults (often called soft faults) such as chafed wires, corroded connectors, or holes in wire shields return very small reflections, often on the order of 10^{-6} of the original signal. The length of the fault also controls the detectability of the fault. A reflection occurs at the front of the fault, and another of approximately equal and opposite magnitude occurs at the back end of the fault. These two reflections overlap and cancel each other out for faults that are small in length even if they are significantly large in impedance change [4].

Reflectometry systems can be made sufficiently sensitive to detect hard faults and many soft faults. However, normal background variation in the impedances of unshielded wires such as water on the wires, variation in the orientation of the wire within a bundle, or vibration against a metallic structure can cause reflections that are as large or larger than the reflection from soft faults, thus making it impossible to detect the soft fault within the larger background reflections [4].

Shielded wires, on the other hand, offer a unique opportunity to locate small faults. Their impedance is far more controlled than unshielded, loosely bundled wires, thus dramatically decreasing the background reflectometry noise, and potentially making it possible to detect small faults in shielded cables such as coax or twisted shielded pair (TSP) wires [10]. A

$W_{fault}=3\text{mm}$ wide hole, $L_{fault} = 10\text{mm}$ in length, in the shield of an RG58 cable would return a reflection of less than 0.01%, for instance. Detecting and analyzing this small reflection requires a very high dynamic range test system, which must either detect or ignore the large initial signal and then detect and analyze the smaller returned signal.

This thesis presents a potentially superior method. The incident signal is sent on the inside of a shielded cable, where it will leak out of a shield aperture. Then, the detection system can receive the signal on the outside of the cable, and compare it to the original signal (on the inside of the cable) to determine the location and nature of the fault. This system would not require as large a dynamic range, since it would receive the (large) internal signal separately from the (small) external signal. It can, in fact, use a unique signal such as the pseudo noise (PN) code used in spread spectrum reflectometry systems (S/SSTDTR), [3] which should not be found on the outside of the cable at all. The system can be built to be extremely sensitive, therefore making it possible to locate a small fault in the cable shield.

2.1.2 Coupling of Discrete Pairs in Wiring Bundles

While many transmission line types exist for the purpose of signal integrity, waveguides and shielded coaxial cables for example, the use of unshielded discrete wires is widespread. Discrete wires are typically used for low voltage applications, such as telephone lines or for DC voltages in aircrafts [11]. Over time, all systems are subject to environmental stress and may degrade or break down and maintenance is necessary. A robust method for locating damage to wiring systems is reflectometry [4] [10] [3] [12] [2] [13] [9]. In reflectometry, a signal is transmitted down a transmission line and that signal is subject to environmental effects. While discrete wires, which are often implemented in long bundles, will act as a standard transmission line, the signal integrity decreases as the frequency of operation increases. Along with dispersive effects, these lines are usually in very close proximity to other structures, such as other wires or a ground frame.

Previous evaluations of reflectometry systems have typically neglected cross coupling between the signals on nearby wires. Most aircraft wires are unshielded bundles of tens to hundreds of wires, all randomly bundled together. Coupling and crosstalk is inevitable in these bundles, and is the subject of this paper. When a transmission line is in close proximity to another transmission line or structure, electromagnetic coupling occurs. In microwave engineering, a parallel line coupler allows for power to be transferred from one transmission line to an adjacent one for the purposes of splitting a signal (for power division, use in a mixer or modulator etc.) [14]. A similar type of coupling occurs on adjacent discrete

wires in a bundled structure. This type of coupling is known as crosstalk [6]. Crosstalk is when an unwanted signal is coupled from the transmitting line, the aggressor, to a quiet adjacent transmission line, the victim. In reflectometry, this presents a very unique problem as well as a unique opportunity. If the coupled crosstalk signal on the victim wire reflects off a fault or normal impedance discontinuity and is coupled back onto the aggressor wire (the actual wire under test) the measured reflectometry signal is now a superposition of the desired fault signal and the signal due to the reflections on the victim line. The problem is that this can potentially create false peaks in the waveform that could appear as fault locations while no fault exists on the wire under test. The opportunity is that it could potentially enable faults in multiple wires to be seen from a single test point. If there are 4-parallel wires, a 4-wire ribbon cable for example, crosstalk can occur between the first pair transmission line and the second pair transmission line. When this coupling occurs, the signal will travel down the transmission line and reflect off any unmatched endpoints or faults.

There are two configurations of interest: common reference coupling, and isolated reference coupling. Common reference coupling will be investigated by using a single structure (a wire within the bundle, an airframe, or the shield of a bundle) as the reference for all tests on a wiring structure. Isolated reference coupling utilizes differential testing of individual pairs of wires. In this case, any signal that is common to both wires should be negated; however, since the geometry of the structures is often not symmetric, there will still be a measurable amount of crosstalk (Figure 2.1).

This thesis evaluates both the problems caused by crosstalk coupling and also its potential application for simultaneously testing multiple wires from a single test point. This S/SSTDTR evaluation is performed for two reasons. First, by using multiple PN codes on different wires, S/SSTDTR can control the coupling and crosstalk between various nearby test systems. Second, the S/SSTDTR can be made extremely sensitive by expanding the length of the PN code that is used for testing, thus enabling location of smaller faults and also potentially of faults on nearby lines.

2.2 S/SSTDTR

Sequence Time domain Reflectometry (STDTR) and Spread Spectrum Time domain Reflectometry (SSTDTR) are relatively new types of reflectometry. These methods utilize a pseudo noise (PN) code. STDTR transmits a PN code, while SSTDTR uses a modulated PN code, as shown in Figure 2.2. There are several advantages of using SSTDTR over a more

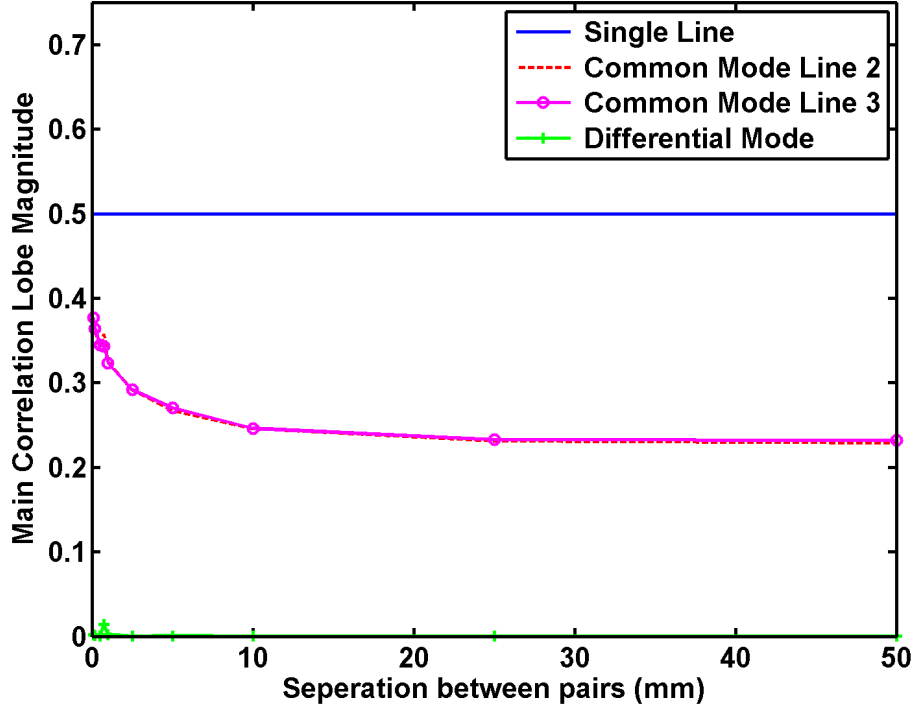


Figure 2.1: STDR correlation coefficient of the main correlation lobe due to coupling vs. distance between two pairs of wires in a 4-wire bundle.

conventional method, such as TDR, which typically utilizes a fast rise step [9]. The first advantage is the fact that the PN code is modulated with a high frequency signal (Figure 2.2). This allows for the signal to be injected onto a live line, 400 Hz power for example, without interfering with the system. The other major advantage is the signal to noise ratio with these methods. When correlating these PN codes, they have a very small correlation coefficient for any lag that is not a periodic multiple of its length; however, this coefficient is dependent on the type of PN code used [2].

There are several types of PN codes: Kasami, Barker, Maximal Length, and Gold codes are some of the common codes used [15]. This thesis will focus on the use of Maximal Length PN codes, or ML codes. An ML code is created by a linear feedback shift register using D-type flip-flops and an XOR gate (Figure 2.3). The input to the shift register, which needs an initial value of 1, is an XOR gate, where the inputs to the XOR gate are specified register tap locations. The choice behind using an ML code lies in its correlation properties. Due to the inherent characteristics associated with the creation of ML codes, they possess a two valued correlation. One value is a 1, when the lag is either 0 or some periodic multiple of its length, and the other is $-\frac{1}{N}$, where N is the length of the PN code (Figure 2.4). In this

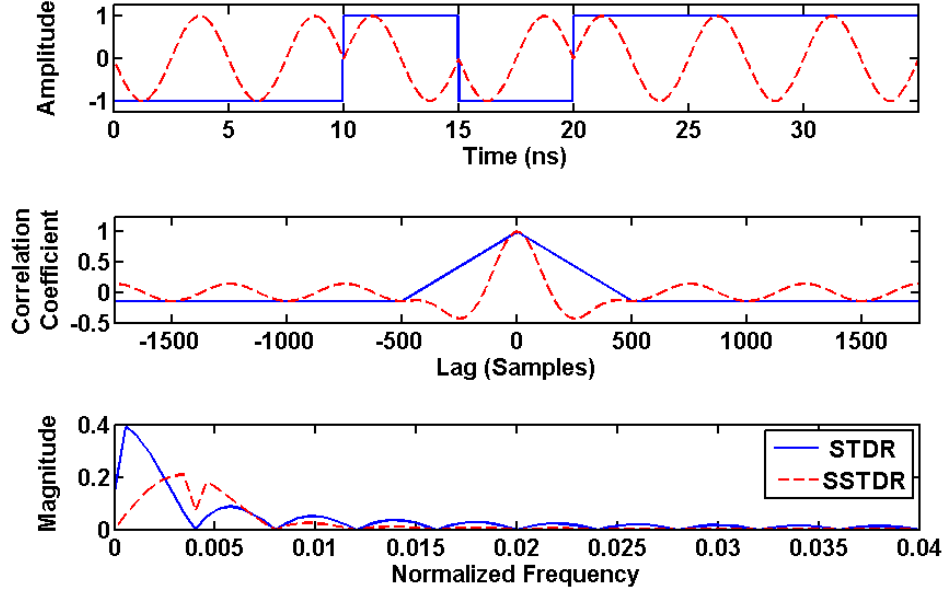


Figure 2.2: STDR (blue solid) and SSTDR (red dashed) time domain waveforms and correlation waveforms. These signals were created using a 200MHz chip rate and a 7-bit ML code.

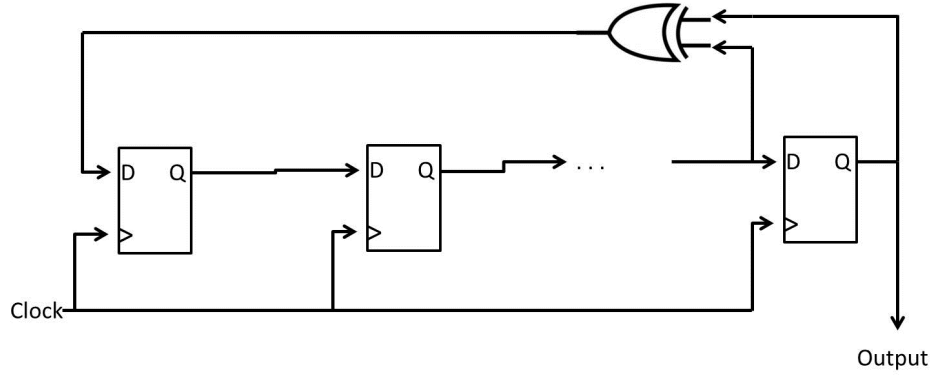


Figure 2.3: Linear Feed Back Shift Register for maximal length PN code generation.

regard, the processing gain obtained by using this type of code increases as the length of the code increases. This is also an advantage in a noisy environment where false faults are observed in conventional reflectometry methods. If a system under test is in a high noise environment, the autocorrelation lobes are still easily detected in the waveform, since noise is often uncorrelated with such a signal (Figure 2.5). As the length of the code increases, the variance of the noise floor (σ^2) decreases. With a longer PN code, faults or perturbations in the waveform become easier to identify. To correlate these PN codes, a circular correlation

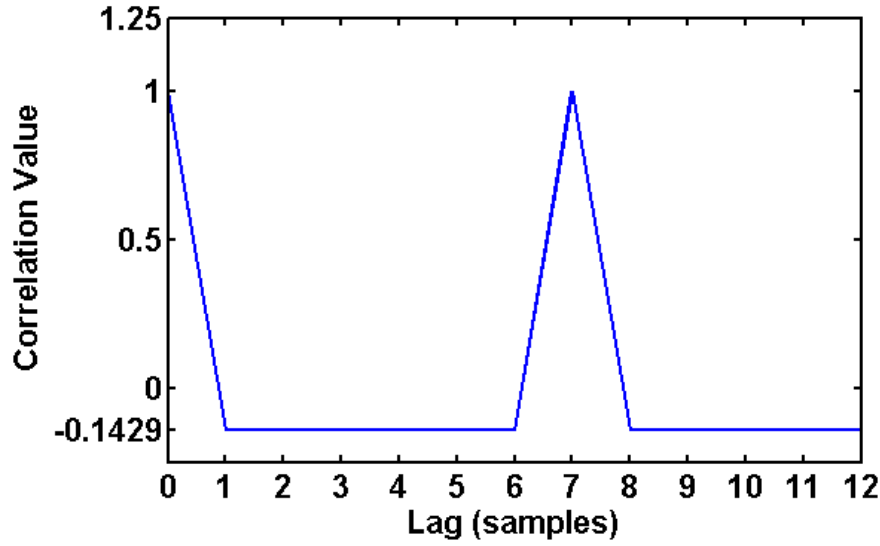


Figure 2.4: Circular correlation of a 7-bit maximal length PN code. At zero lag and any periodic multiple of the PN code length, the correlation value is 1. At any nonperiodic multiple of the PN code length, the correlation value is -0.1429 ($-\frac{1}{N}$).

must be performed.

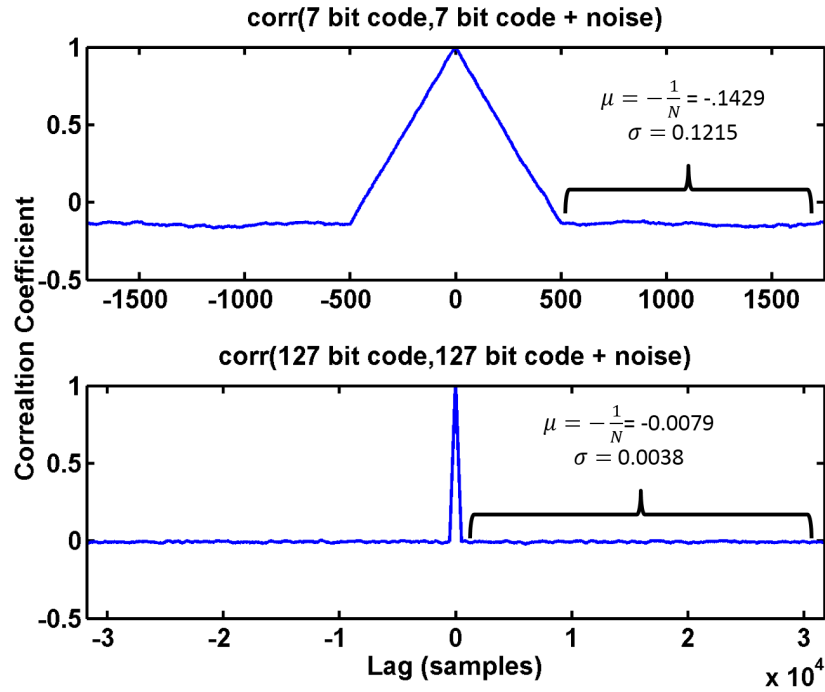


Figure 2.5: The correlation waveform of an ML code correlated with a copy of itself corrupted by additive white Gaussian noise of zero mean and unit variance.

2.2.1 Correlation Methods

In order to correlate a PN code, a circular correlation must be performed. The general correlation coefficient (ρ) is defined by a normalized integral of the product of two signals (Equation 2.1).

$$\rho(t) = \frac{1}{N} \int_{\tau=-\infty}^{\tau=\infty} x(\tau)y(t+\tau)d\tau \quad (2.1)$$

This can also be thought of as a sliding integral. It is similar to a convolution; however, the second sequence is not flipped in time. Many algorithms will zero pad the beginning of the sequence; however, this is a problem for correlating a PN code (Figure 2.6). The PN code has unique correlation properties that will not be preserved unless a *circular correlation* is performed rather than zero padding either sequence. In order to accurately perform this circular correlation, the S/SSTDTR signal must be transmitted continuously. That is when the excitation reaches the end of the sequence, the sequence must start over and transmit again. This algorithm is easily accomplished by simply shifting the longer of the two sequences, and performing a dot product on the two sequences. While this is a simple and straightforward method of correlation, as a recursive operation in postprocessing, it can

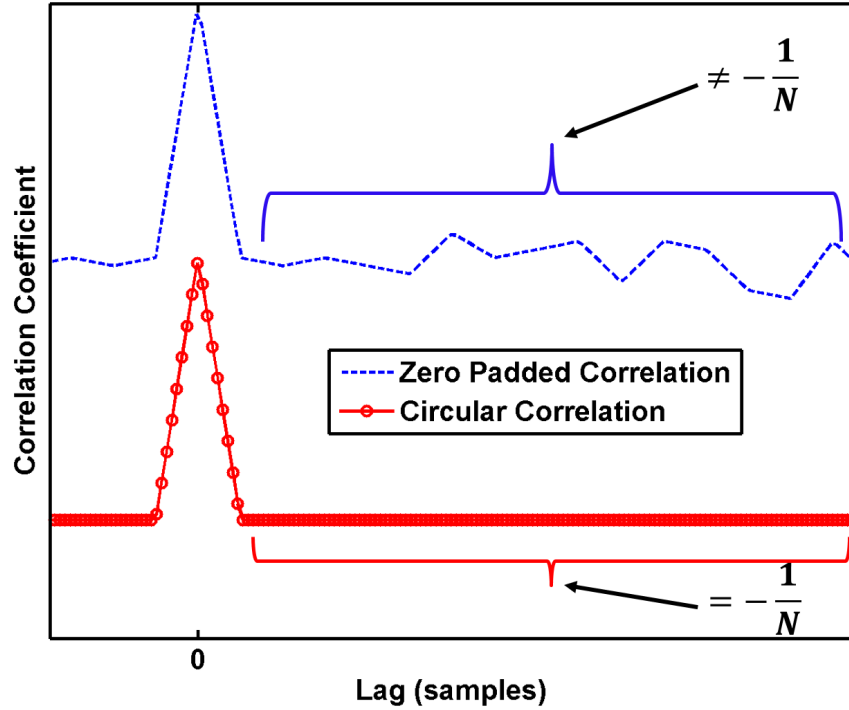


Figure 2.6: Comparison of performing a zero padded correlation on an STDR sequence (blue dashed line) vs. a circular correlation (red solid line).

be quite slow. The correlator used for the analysis in this paper is an *fft* implementation of the correlation (Equation 2.2).

$$\rho(t) = \mathcal{F}^{-1}(X(\omega) \cdot Y^*(\omega)) \quad (2.2)$$

Using this correlation technique, the correlation is still circular (ensured by taking an N point *fft* for an N length excitation) but is much faster than the brute force method of shift, multiply, and sum. This correlation can take place in either software or hardware. For this thesis, all correlations and other postprocessing takes place in software.

2.3 Simulation Methods

This thesis models two separate systems: a shielded coaxial cable (coupling via apertures) and an unshielded discrete wiring bundle. These systems were modeled using different software.

2.3.1 Modeling Shield Apertures

To simulate a shield aperture, a prepackaged full wave solver was used. Using CST, *Computer Simulation Technology*, a 3D model was constructed of a coaxial cable with a shield aperture and simulated via FDTD. This software is an FIT solver which has desirable convergence behavior; however, it is very time and resource intensive. An accurate method was needed to model the fields accurately, both internal and external to the cable, in order to obtain the electric and magnetic fields associated with propagation through this small aperture. Once the fields were obtained from the simulation, postprocessing was performed on the internal and external (transmitted through the aperture) fields to obtain the frequency spectra of the shield apertures. This information is applied to the design of the toroidal sensor for localizing the apertures. The sensor is optimized to operate in the frequency range that is applicable to the signal escaping from the aperture when the cable is excited. This sensor and the aperture characteristics are described in Chapter 3.

2.3.2 Modeling Discrete Wiring Structures

Transmission line coupling occurs through two mechanisms. When these lines are in close proximity to one another, they share a mutual inductance, L_m , and mutual capacitance, C_m [6] [16]. These mechanisms dictate the magnitude and frequency response of the coupling. At low frequencies, the mutual inductance will be the dominating factor, while at higher frequencies, the mutual capacitance will be the stronger contributing factor. This type of coupling can be detrimental (increased noise and interference in picking a fault signature

in the correlation waveform) or advantageous (coupling to adjacent wires can allow for simultaneous testing of multiple wires). Another issue is the length of the transmission lines. In aerospace applications, a bundle of wires can contain tens of feet of parallel wires or longer. Two parallel structures will have a capacitive coupling effect that is proportional to the length of the wires [13]. As the wires become longer, the capacitive coupling becomes greater. For long bundled structures, the crosstalk can be significant.

The frequency spectra of the test signal is very important in this evaluation of transmission line coupling since this type of coupling is frequency dependent. Higher frequencies will couple well while low frequencies will couple poorly or not at all. This filtering effect is similar to a high pass filter, which is also a differentiation of the signal in time. While both S/SSTDR are broadband signals, STDR has a DC component whereas SSTDR does not (Figure 2.2). Since the SSTDR signal has less low frequency content and the coupling from one transmission line to the other is a high pass filtering effect, more of the SSTDR signal will couple to adjacent transmission lines and structures than the STDR signal.

To obtain the coupled signals from one transmission line to another, an advanced forward model was used. A packaged full wave 3D electromagnetic solver is not preferred for this modeling due to the time consumption and resources needed to perform the computations. For the modeling of discrete wiring structures, MATLAB was used to develop the algorithm employed. Previous work to model complex wiring faults has been performed by using forward models. The method employed for this thesis is similar to that of [12]. The wiring structure is modeled using an FDM solver, *Finite Difference Method*. This will solve the system for the necessary coupling parameters, L_m and C_m , as well as the characteristic transmission line L and C parameters by modeling a 2D cross-sectional area of the wiring structure. Once known, the transmission line parameters can then be used to model the wiring structure in the time domain by means of a 1D FDTD model, *Finite Difference Time domain*, derived from the telegrapher's equations. FDTD is a very robust and versatile method for simulating time domain systems [17]. The other advantage of using this 1D model is the computational simplicity compared to a 3D full wave solver. Using this 1D model, both STDR and SSTDR waveforms can be simulated for analysis of the coupling effects due to the presence of multiconductor structures. Wiring faults are easily simulated by implementing a short circuit or open circuit. These faults can occur between a single wire and the system reference conductor or between one nonreference conductor and an adjacent one. Discrete wiring coupling and reflectometry crosstalk is the topic of Chapter 4.

2.4 Proposed Method of Fault Location

In order to localize a small shield aperture, the signal is placed on the internal connector of a shielded cable, propagates down the cable, and escapes through a hole in the shield. It then propagates along the outside of the cable (in both directions), where it can be picked up by a toroidal coupler (Figure 2.7). The delay between the internal and external signals is used to determine the distance to the fault. The size of the fault can be detected by both the magnitude of the external signal and its frequency spectra.

To qualify the effects of coupling crosstalk on discrete wiring structures in S/SSTDR, a signal will be excited between a single wire and a system reference conductor. The signal will then be measured on all nonreference conductors. These signals will then be correlated with the original excitation in order to isolate the fault signatures that appear on adjacent wires within a bundled structure. This analysis will be performed for a bundled structure while using a common reference to all conductors. Additionally, a separate analysis in which the conductors do not share a common signal reference with one another will be conducted on the same wiring structure.

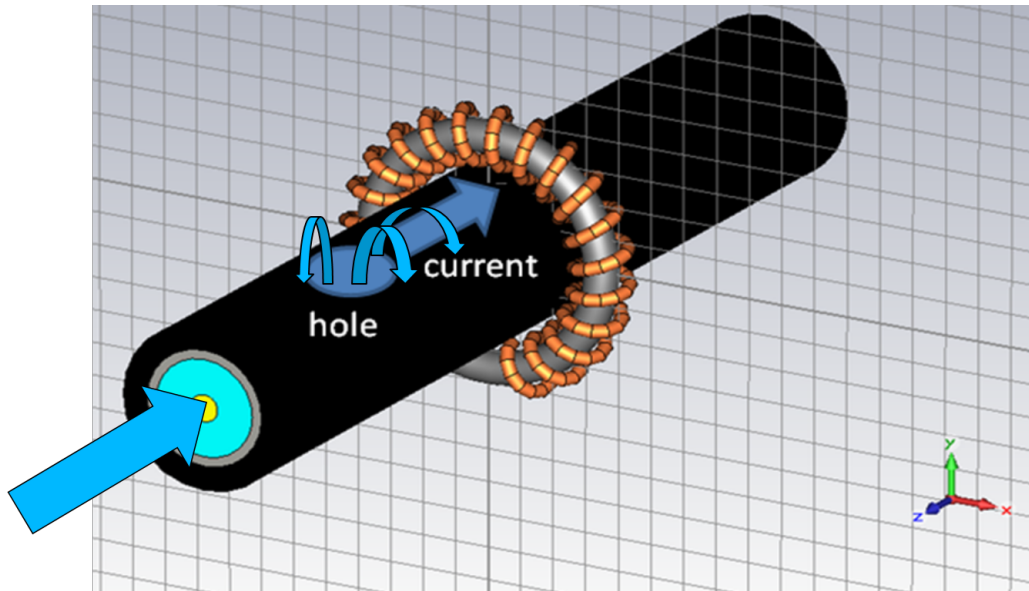


Figure 2.7: RG-58 coaxial cable with a toroidal sensor for detecting signals leaking from a fault.

CHAPTER 3

LOCATING SMALL APERTURES IN CABLE SHIELDING

This chapter describes a method for detecting and locating faults on cable shields using an adapted reflectometry system that transmits a signal on the internal conductor and senses the very small signal leaking to the outside of the shield, correlated with the original signal inside the cable. The signals that leak out of the hole as in the damaged shield and propagate down the outside of the cable are quantified as a function of hole size and frequency. A ferrite loaded toroidal sensor is also designed and quantified for receiving the external signal and relating it to the internal signal in order to both detect and locate the shield damage. Both simulations and measurements validate the effectiveness of this method. An example configuration demonstrates the ability to locate 5mm long x 4mm wide fault on RG58 coax to within ± 2 cm on a two meter cable.

3.1 Fields Leaking from a Shield Aperture

When a small hole in cable shielding occurs, electromagnetic fields can leak from the fault, as shown in Figure 3.1. To find the frequency range and magnitude of the fields that will escape these small holes, such as jacket and shielding frays, Bethe's hole theory can be applied [18] [19]. Frays acting as these small holes, which have a poor low frequency response and a stronger response at high frequencies, act like high pass filters, where only high frequencies are coupled onto the outside of the cable. This, in effect, differentiates the original signal that was on the inside of the cable.

This interesting effect can be seen in the simulation of a signal propagating down an RG58 coaxial transmission line, and then escaping through a $W_{fault}=4$ mm wide by $L_{fault}=10$ mm long aperture in its outer jacket and shielding. The transmission line was excited by a 1 watt Gaussian pulse with a 3GHz bandwidth. The magnetic field was evaluated at various points along the length of the cable, shown in Figure 3.2, as marked with an "x" starting at $z=0$ mm directly over the fault.

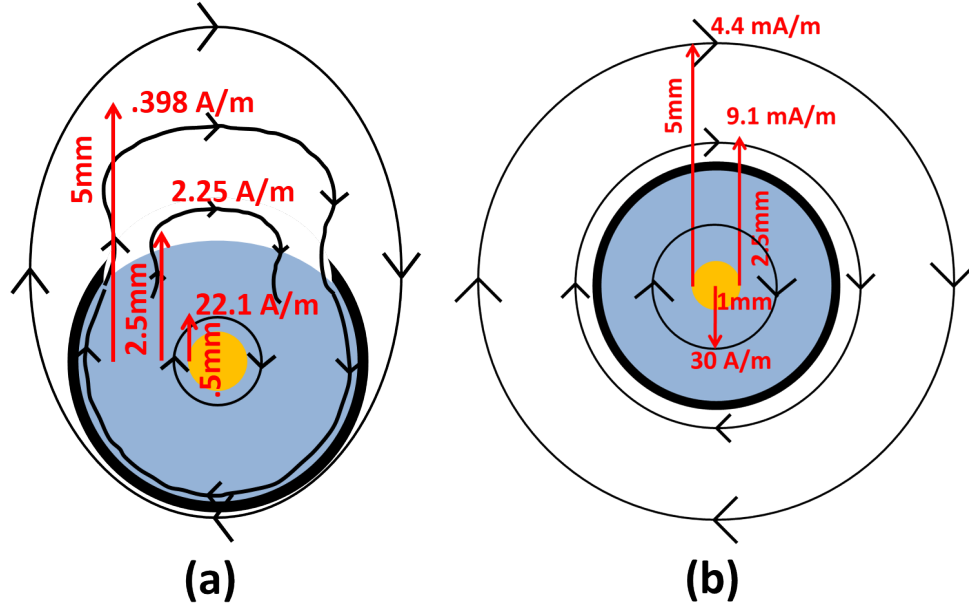


Figure 3.1: Circulating magnetic field propagating down an RG58 coaxial cable due to a shield fault $W_{fault}=4$ mm wide and $L_{fault}=10$ mm long. The field was sampled at the fault location, $z=0$ mm (a), and at $z=250$ mm away from the fault (b).

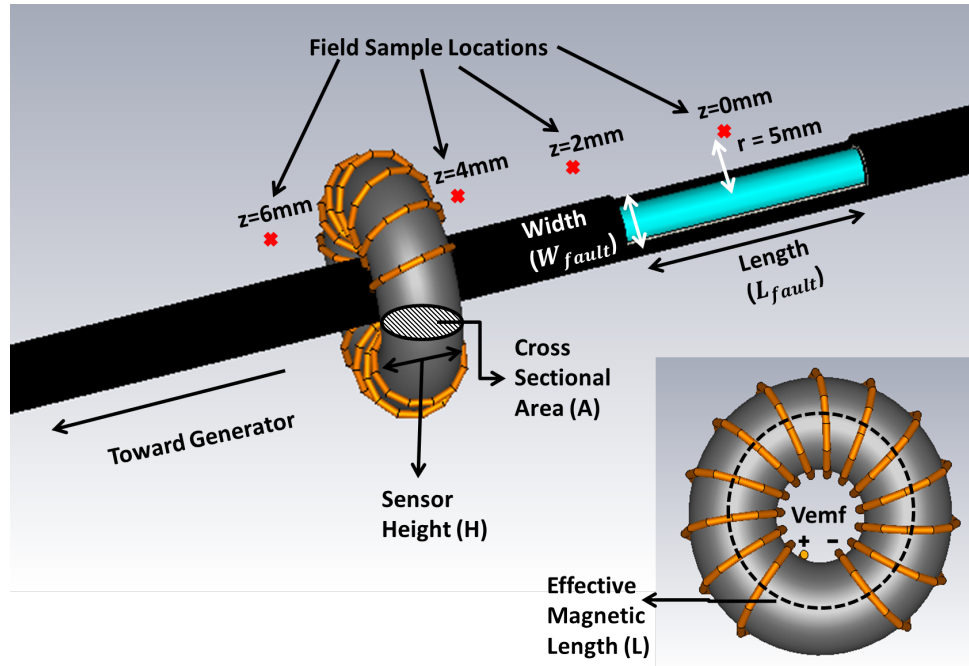


Figure 3.2: Toroid sensor for picking up the signal that leaks out of the fault and propagates down the outside of the cable shield.

Prior to reaching the fault, the magnetic field strength is 30 A/m. At the fault location, even near the center conductor, the magnetic field strength is 22.1 A/m, over 25% lower. Directly above the fault, $z=0\text{mm}$ and $r=5\text{mm}$, the magnetic field strength is less than .4A/m, only 1% of the original field strength. The magnetic field strength is of particular interest since the toroid acts as an inductive pickup and will be measuring the magnetic field. The signal just above the hole ($r=5\text{mm}$ above the shield) retains its original Gaussian shape, as shown in Figure 3.3 (the $z=0\text{mm}$ curve).

However, as the signal moves away from the hole, towards the end of the cable in the direction of propagation, it transforms into the derivative of the original signal (the $z=4\text{mm}$ and $z=6\text{mm}$ curves, for example). The signal also decays very quickly. Prior to incident on the fault, the electric field strength is approximately 7000V/m. At the fault location, $z=0\text{mm}$, and immediately above the cable, $r=5\text{mm}$, the electric field strength is less than 50V/m, less than 1% of the original field strength. Once the signal has coupled to the outside of the cable, this differentiated signal propagates until it attenuates or is reflected. Once in the propagating region, the attenuation is minimal for this cable and environment, as the jacket material is low loss. If the cable were in a lossy environment (water for example), the expected attenuation would be more significant. For any lossy environment,

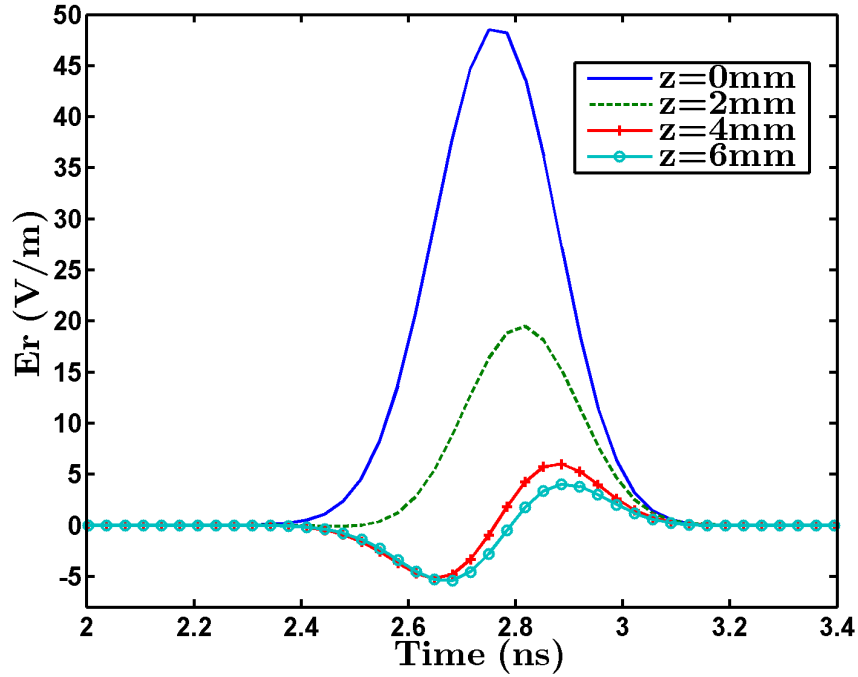


Figure 3.3: Observed waveform along the cable $r=5\text{mm}$ above the shield. $z=0\text{mm}$ marks the fault location, and the other curves are further from the fault, as shown in Figure 3.2.

we can expect the attenuation on the cable to act like a low pass filter, attenuating the higher frequencies more than the lower frequencies.

The magnitude of the reflected signal and its frequency response are controlled by the size of the aperture in the shield. The ratio of the aperture width to the incident wavelength will impact the magnitude of the signal exterior to the fault [20] [21]. The fault width will determine the characteristic impedance of the fault section of cable and will have very little impact on the magnitude of the transmitted signal through the aperture while the length of the fault dictates how much signal is coupled to the exterior of the cable and contributes very little to the change in impedance [20] [12].

In order to demonstrate the frequency response of the fault, an $L_{fault}=10\text{mm}$ long fault was made in the shield of an RG58 cable and the width was varied from $W_{fault}=1\text{mm}$ to approximately the width of the cable, $W_{fault}\approx 5\text{mm}$. The radial electric field, $E_r(\text{external})$, was sampled at a distance of $r=5\text{mm}$ above the center of the cable and $z=250\text{mm}$ away from the fault. Another sample, $E_r(\text{internal})$, was taken at $r=1\text{mm}$ (at the inner conductor) and $z=250\text{mm}$ away from the fault location. The ratio of the frequency spectra was computed for the two samples to obtain the fault response. The observed effect (Figure 3.4) shows an increase in magnitude of the external signal as the fault width is increased and a stronger

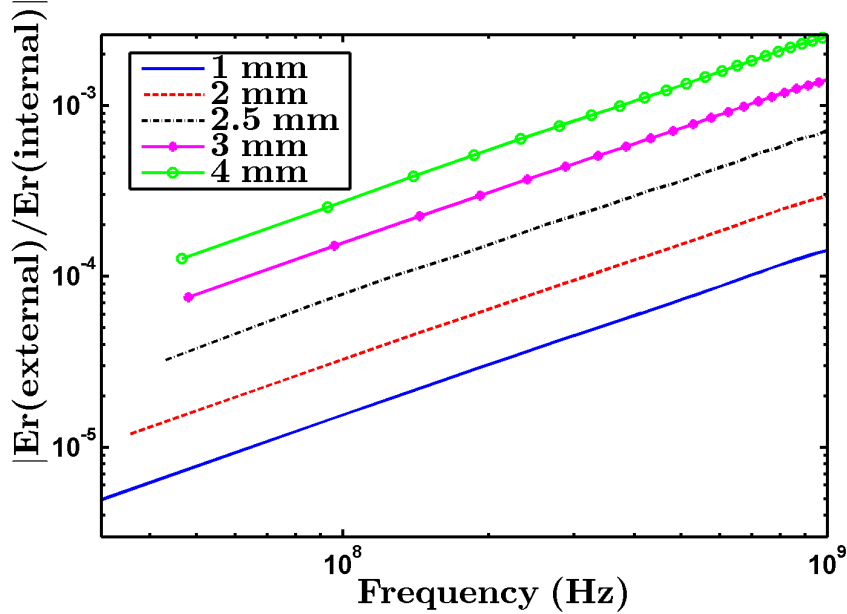


Figure 3.4: Fault response of an $L_{fault}=10\text{mm}$ long fault for various fault widths from $W_{fault}=1\text{mm}$ to 4mm .

response at higher frequencies for all aperture sizes, as expected. A similar case was investigated for a $W_{fault}=3\text{mm}$ wide fault but with different lengths, shown in Figure 3.5. As the fault becomes very large, lower frequencies have a stronger presence. The aperture acts as a high pass filter, as expected, with the specific frequency response being dependent on the size of the fault. The fault responses shown in Figure 3.4 and Figure 3.5 are for rectangular chafes. Results for oval chafes are similar.

3.2 External Propagation

The fault location system described in this paper is a modified version of reflectometry. Rather than detecting the reflected return signal, the signal that escapes from the cable is detected and compared to the incident signal on the inside of the cable to determine the distance to fault. The measured time delay is converted to distance using the velocities of propagation (VOP) on the inside and outside of the cable, which are different.

The velocity of propagation on the inside of the cable is a function of the size, shape, and materials in the cable, and is well known for standard types of cable including coax [22]. For most practical cables, it is about $\frac{2}{3}$ the speed of light. The velocity on the outside of the cable is not as well documented, and it should be nearer to the speed of light, since

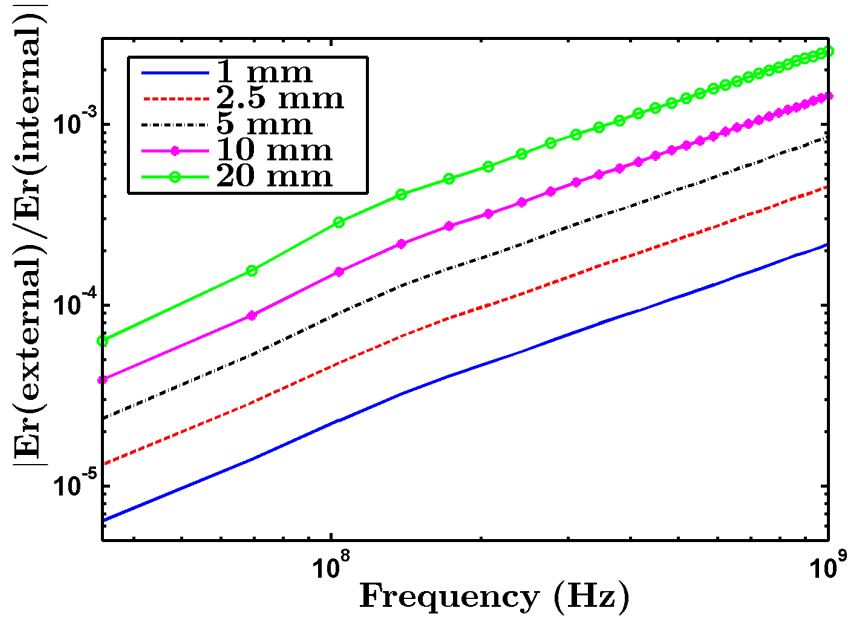


Figure 3.5: Fault response of a $W_{fault}=3\text{mm}$ wide fault for various fault lengths from $L_{fault}=1\text{mm}$ to 20mm .

most of the signal is propagating in the air around the cable. The VOP for this application, where the signal propagates down the cable and then escapes and propagates on the outside of the shield, is a linear combination of the two.

To determine the VOP, both simulation and measurements were performed. To measure the VOP, an undamaged section of cable was used and two toroidal sensors, as described in Section 3.3, were placed around the cable starting 0.5 meters apart. Using a 500ps rise time square pulse, 0.5 volts in amplitude, the signal was transmitted with one toroid and received with the second. The transmitted pulse was used to trigger an oscilloscope to capture both waveforms. RG58 coaxial cables of the same length were used for both sensors and to trigger the oscilloscope in order to ensure the delay was equal from the generator to the toroid and the oscilloscope to the toroid. Measurements were taken at 12.7 cm intervals, shown on the vertical axis of Figure 3.6. The corresponding time delay, shown on the horizontal axis of Figure 3.6, was determined using a sliding correlator to accurately identify the rising edge of the pulse [15]. Using a linear fit, the measured VOP was found to be $0.92c$, where c is the speed of light in free space. The median value of the raw data was $0.937c$. Both of these measured values are close to the simulated value, $0.94c$ [23]. The simulation was performed using CST, *Computer Simulation Technology*. A 3GHz 1 watt Gaussian pulse was used to

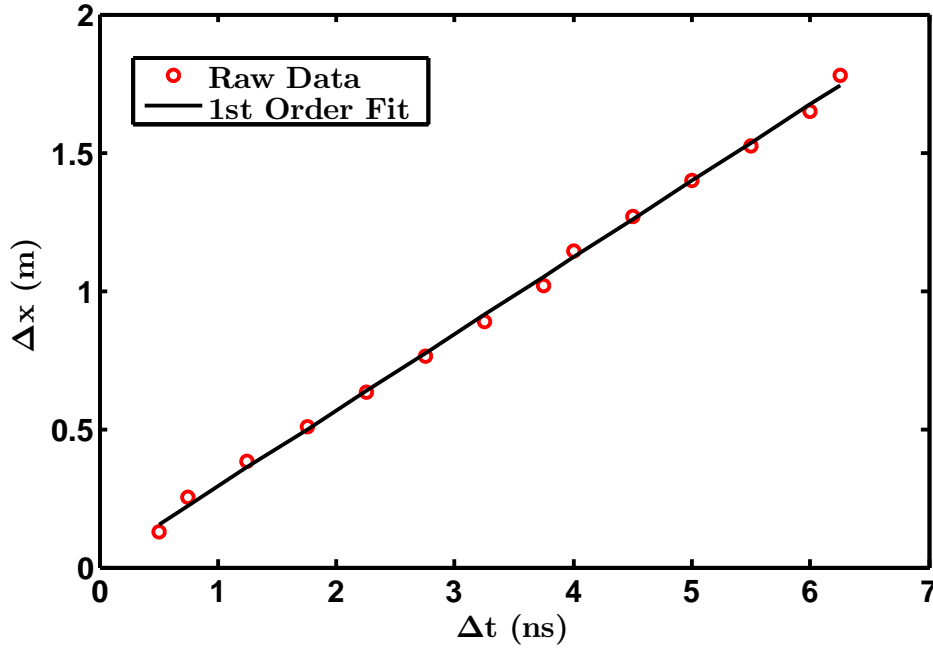


Figure 3.6: Measured velocity of propagation for a signal traveling along the outside of an RG58 cable.

excite the system. The radial electric field component was sampled at several points on the outside of the cable. Based on the time delay calculated from one measurement to the next, the simulated VOP was $0.94c$.

In order to facilitate future modeling of the propagation behavior on the exterior of a coaxial cable, a parameter extraction method was used to determine the RLGC parameters for external propagation from simulated data. The method of the parameter extraction used is described in [24]. To perform the extraction, the fields external to the cable were measured at $r=5\text{mm}$ above the cable and at $\lambda/8$ increments. Time harmonic sinusoidal signals were used to excite the cable stepping from 100 MHz to 1 GHz. From the field data, the wave impedance Z , the attenuation constant α , and the propagation constant β are calculated. The RLGC parameters in Figure 3.7 can then be found from Z , α , and β . Table 3.1 contains the values at 200 MHz (a 200 MHz sinusoidal signal was used for aperture detection). The velocity of propagation from the parameter extraction was calculated using:

$$VOP = \frac{2\pi f \text{ meters}}{\beta \text{ seconds}} \quad (3.1)$$

where f is the frequency in hertz and β is the propagation constant in radians/meter. The median value of the velocity of propagation calculated this way was $0.927c$. This falls between both the measured values; however, it was almost 1.5% lower than the value

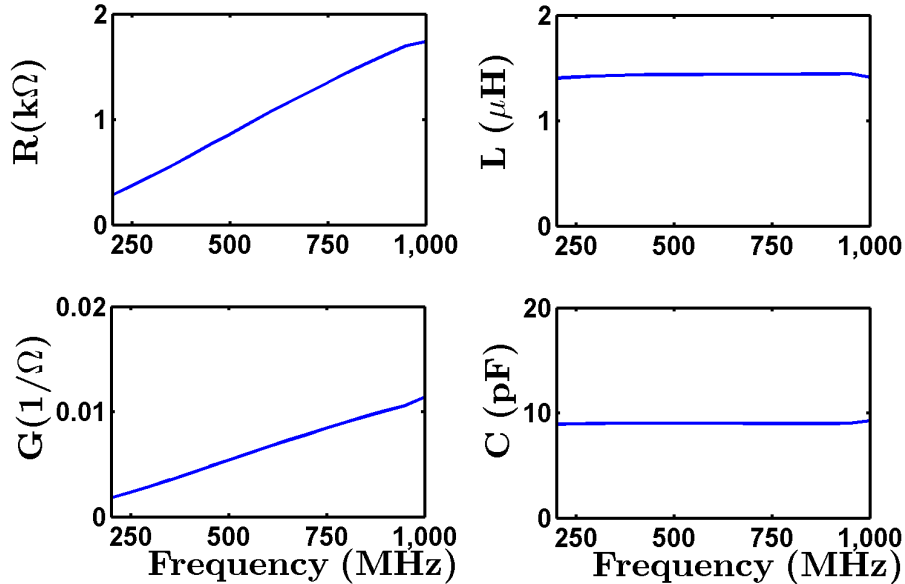


Figure 3.7: Calculated RLGC parameters for external RG58 propagation.

Table 3.1: Extracted RLGC Parameters

$\mathbf{Z}_o(\Omega)$	396
$\mathbf{R}(\Omega)$	280
$\mathbf{L}(\mu\mathbf{H})$	1.4
$\mathbf{G}(\frac{1}{k\Omega})$	1.8
$\mathbf{C}(\text{pF})$	8.9

observed in previous simulations, 0.94c. This section has described and quantified the fields that escape through an aperture in the shield and how they propagate down the cable. The next section will describe a toroidal sensor that can be used to pick up these fields.

3.3 Sensor Characterization

In order to receive the fields that have leaked to the outside of the cable, and return them for processing, a direct connection to the cable could be made (making metal-to-metal contact), or a noncontact sensor could be utilized. The direct contact system could certainly be made to work well; however, it would be more invasive and therefore require more specialized connection to the system under test. For this study, the noncontact toroidal sensor was used, as shown in Figure 3.2.

The two methods for noncontact coupling are capacitive coupling and inductive coupling. Inductive coupling utilizes the magnetic field while capacitive coupling utilizes the electric field [25]. There are several types of capacitive couplers, including the concentric ring or cylinder, parallel wires, or coils around the wire under test [13]. Inductive coupling can be done with toroids (Figure 3.2) and other ferrite pick-up devices, and is the method used in this paper. A toroid is placed around the wire. The ferrite inner core receives and augments the magnetic field circulating around the outside of the shield. The coil of wire around the core picks up the magnetic field, and converts it to an electromotive voltage, V_{emf} [26].

The goal of the sensor design is to maximize the received signal. The induced signal on the sensor is governed by Faraday's law:

$$V_{emf} = -NA\mu_o\mu_i \frac{\partial \mathbf{H}}{\partial t} \quad (3.2)$$

The induced voltage, V_{emf} , will be proportional to the number of turns, N , the magnetic permeability of the ferrite, μ_i , the cross-sectional area of the ferrite, A , and the derivative of the magnetic field, $\frac{\partial \mathbf{H}}{\partial t}$, (which is largest near the shield). In this system, the toroid acts as a high pass filter. The parameters that can be optimized are the number of windings, N , (the more the better, until resistive losses reduce the efficiency of the system), the gauge of the

windings (thinner gauge wire will allow for additional turns; however, larger diameter wire will have less resistive losses), the geometry of the sensor (a larger core, A , will concentrate more magnetic flux), and the material of the core, μ_i , which will determine the frequency response of the toroid. To characterize the sensor, each parameter was varied. The toroid was placed around a stranded section of 6 AWG copper conductor wrapped in polyimide. The conductor was then excited with a fast rise voltage step function (500ps at 0.5 volts) and the toroidal sensor response was measured with an oscilloscope.

3.3.1 Windings

Theoretically, the induced emf is proportional to the number of windings, N . However, the parasitic resistance and capacitance will increase with each turn. A CN20 core ($\mu_i=925$, $L=55\text{mm}$, $A=64\ \mu\text{m}^2$) was excited with a fast rise square pulse. The number of windings was varied. As the number of turns increases, the received signal magnitude increases, but the response becomes underdamped, as shown in Figure 3.8. This is because of the high pass nature of the toroid. The high pass filtering effect will also differentiate the pulse used to excite the material. The voltage is also on the same order of magnitude as the excitation. While there are filtering effects from the toroid, the higher permeability of the core material (μ_i) will concentrate more flux and a higher than unity number of turns ($N > 1$) will cause

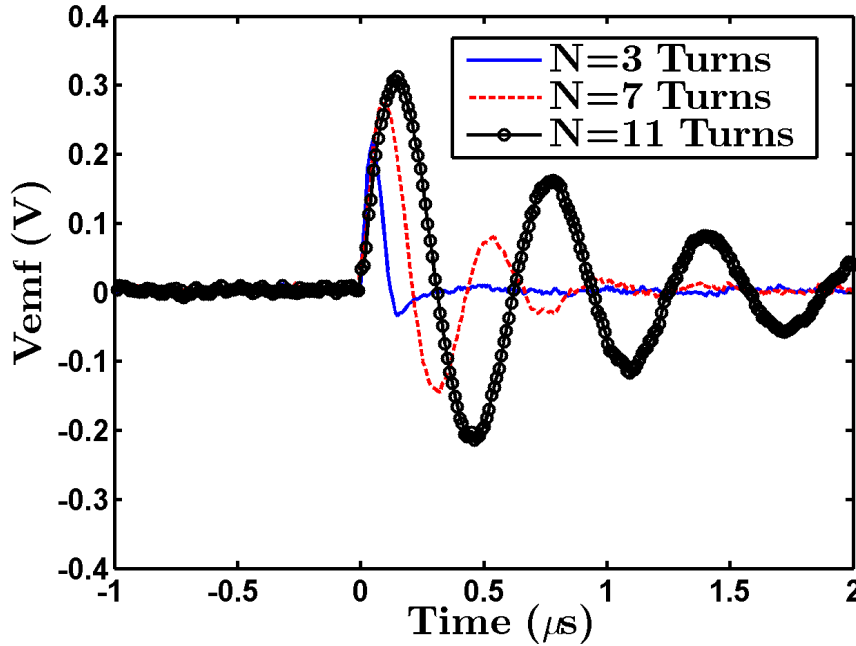


Figure 3.8: Step response for CN20 core with varied number of windings. $\mu_i=925$, $L=55\text{mm}$, $A=64\ \mu\text{m}^2$.

amplification of the fields being measured. Damping with discrete components can be performed on the sensor to negate the underdamped effects of the additional windings; however, resistive components would dissipate the power of the induced signal, and are therefore not ideal.

3.3.2 Wire Gauge

As the wire diameter decreases or the frequency of operation increases, attenuation became more noticeable. At $f=200$ MHz, attenuation was noticeable on 32 AWG. For the frequencies used in this system ($f \leq 200$ MHz), the observed attenuation in measurements were negligible with 30 AWG or larger for the windings.

3.3.3 Geometry

The V_{emf} is proportional to the cross-sectional area of the sensor, A , and the strength of the derivative magnetic field, $\frac{\partial \mathbf{H}}{\partial t}$. To examine the geometry of the sensor, two parameters were varied individually: the cross-sectional area, A , and the effective magnetic length, L , both of which are illustrated in Figure 3.2.

3.3.3.1 Cross-Sectional Area

Two cores, one with approximately twice the cross-sectional area of the other, were excited. The small of the two cores had an area of $A=64\mu\text{m}^2$ while the larger core cross-sectional area was $A=128\mu\text{m}^2$. The cross-sectional area of the larger core was doubled by using a core with approximately twice the height, H . The excitation signal was a step function with a rise time of 500ps to 0.5 volts. Since the induced signal is proportional to the cross-sectional area, where the magnetic field will be concentrated, the signal should have increased by a factor of two. The resulting signal, shown in Figure 3.9, was significantly larger but not twice as large for the doubled cross-sectional area due to damping effects of the toroid. A more underdamped response was also observed, and this contributed to the difference in magnitude from what was expected.

3.3.3.2 Effective Magnetic Length

In order to evaluate the impact of the effective magnetic length, again two cores were selected, one with approximately half the magnetic length of the other, and both samples were excited using the same step function as with the previous section. The smaller core selection had the same height, and the inner and outer diameter were approximately half the size of the larger core. The induced signal is proportional to the strength of the magnetic

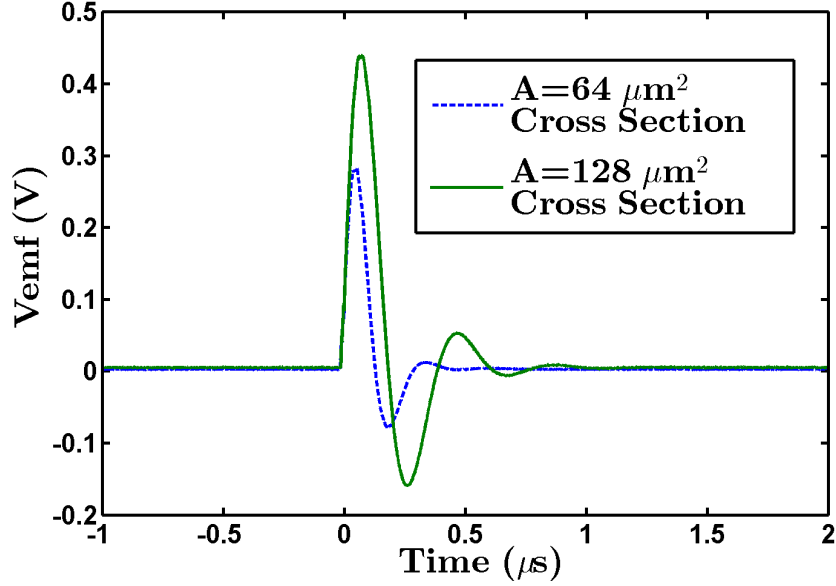


Figure 3.9: Step response of different cross-sectional area on a CN20 ($\mu_i=925$) core with 5 turns.

field. As the effective magnetic length increases, the distance from the source, or in this case the wire under test, increases and the strength of the magnetic field decreases. The magnetic field strength will decrease since it is proportional to $\frac{1}{r}$. Figure 3.10 illustrates this effect. The response was more underdamped with a smaller magnetic length, but the magnitude of the received signal was significantly larger. The magnetic length should be as small as possible while still allowing for enough room to accommodate the wire under test and a layer of windings between the inner surface of the core and the wire under test.

3.3.4 Materials

The ideal material properties for a soft ferrite include a low hysteresis loss, a low coercive force, high resistivity, and a high initial and maximum permeability (μ_i) [27]. Finding a material with all of these ideal characteristics can be difficult. A high resistivity, to reduce eddy current losses, and a low coercive force, to allow changes in magnetization under the influence of a small signal, were the driving characteristics in material selection for this sensor. The two materials selected for characterization were an N40 core and a CN20 core. While both selections are a Nickel Zinc material, the CN20 has an initial permeability of $\mu_i=925$ and a coercive force of 0.2 Oersted, while the N40 has an initial permeability of

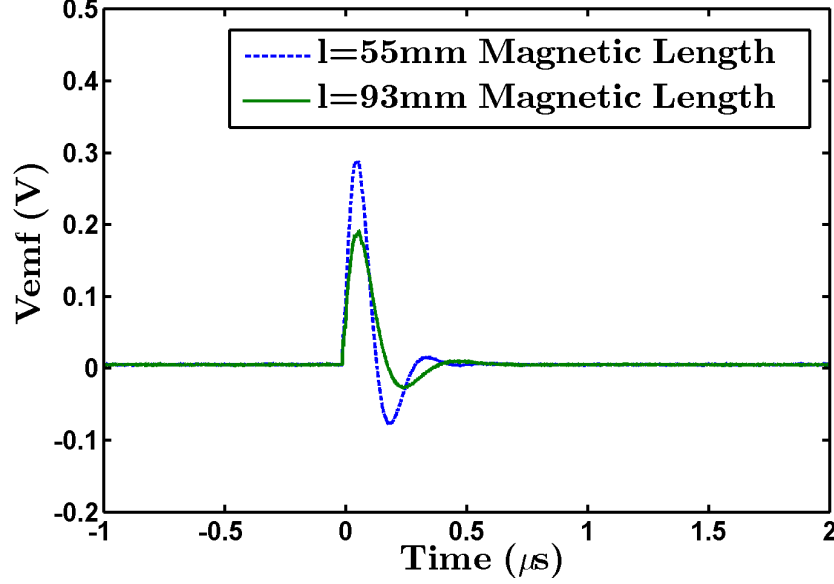


Figure 3.10: Step response of different magnetic lengths on a CN20 ($\mu_i=925$) core with 5 turns.

$\mu_i=15$ and a coercive force of 8 Oersted. Both core materials have a resistivity of $10^{10}\Omega$ cm [28]. In order to characterize the material properties, both frequency domain and time domain characteristics were considered. For time domain characterization, each core was wound with 5 turns of 24 AWG solid core wire with magnetic length $L=53\text{mm}$, and cross-sectional area $A=64\mu\text{m}^2$. The step responses are shown in Figure 3.11. While the CN20 material does have a much larger response, it also has a very long relaxation time and low frequency response while the N40 has much higher frequency content. The N40 will also operate at much higher frequencies. The CN20 will suffer dispersion effects at lower frequencies and begin to choke the signal rather than detect it. Since the aperture acts as a high pass filter, the highest possible test frequency for localization is ideal. In order to use higher frequencies, a high frequency material must be used in the sensor core. The N40 material was chosen because it has better high frequency characteristics than the CN20 material.

3.3.5 Sensor Specifications

The toroidal sensor used in the remaining tests in this paper consisted of 9 turns of 24 AWG solid core wire around an N40 core (chosen for its high frequency properties and an

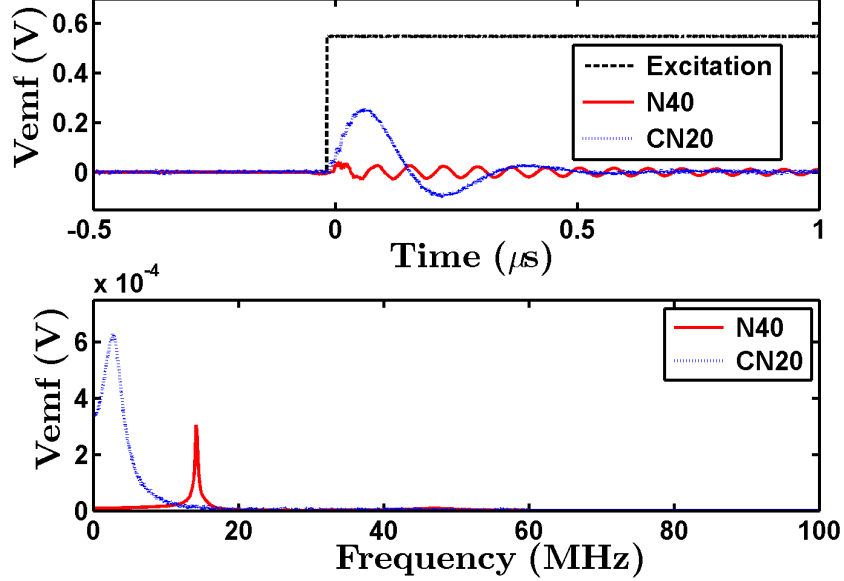


Figure 3.11: Measured step response comparison of N40 ($\mu_i=15$) and CN20 ($\mu_i=925$) core materials. Both core selections are of the same dimensions ($A=64\mu\text{m}^2$, $L=53\text{mm}$) and number of windings ($N = 5$) using 24 AWG wire.

initial permeability $\mu_i=15$). The cross-sectional area and effective magnetic length were $A = 64\mu\text{m}^2$ and $L = 28\text{mm}$, respectively. A small height was required since the faults to be localized are small. If the sensor is too long, directly over the fault, the net flux in the core material would have been approximately zero since the fields are going in opposing directions on opposite sides of the aperture.

3.4 Aperture Localization

Once the sensor was characterized, a $L_{\text{fault}}=10\text{mm}$ long $W_{\text{fault}}=4\text{mm}$ wide fault was made in the center of a two meter RG58 coaxial cable. The cable impedance was 50Ω and excited by a 50Ω generator terminated with a 50Ω load. The toroid was placed directly over the fault and then moved in $z=0.5\text{cm}$ increments toward the generator. A larger V_{emf} was measured for higher frequencies and directly over the fault, there is a low measurement (Figure 3.12). This will occur when the size of the sensor is close to the size of the fault. When the fields escape the cable, they propagate in both directions, toward the generator and toward the load. The magnetic field traveling toward the load will have the opposite polarity as the magnetic field traveling toward the generator. If the sensor is placed directly

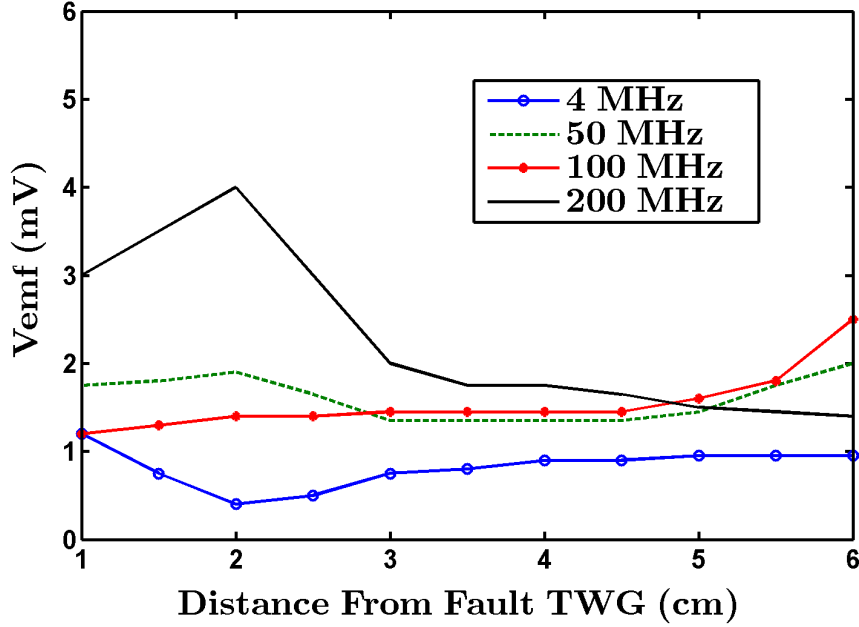


Figure 3.12: Measured frequency response of a $L_{fault}=10\text{mm}$ long $W_{fault}=4\text{mm}$ wide fault. The measurements were made by moving the toroid at $z=0.5\text{cm}$ increments toward the generator (TWG). $z=1\text{cm}$ on the horizontal axis is 1cm away from the fault.

over the fault, both fields will interact with the ferrite core, and the net flux within the core will be zero.

Next, a fault, $L_{fault}=5\text{mm}$ long by $W_{fault}=3\text{mm}$ wide, was made at various locations. A 200 MHz 1Vpp sinusoidal wave was used for localization. The generator, load termination, and cable impedances were 50Ω . A base line (no fault) measurement was taken, a fault was made, and then the measurement was performed again. The results are shown in Figure 3.13. The fault signal was calculated by taking the difference of the two measured V_{emf} signals. Reflections from the generator and load ends of the cable were observed. These reflections occur on the outside of the cable and are expected since the external transmission line (the cable jacket) was not matched at the end points. When the fault was made close to the load, reflections from the load made localization more difficult, but the faults were still observable. As the magnitude of the reflections increased at the end points, near the generator and the load, the magnitude of the fault signal was reduced beyond the noise floor. The fault length was then increased to $L_{fault}=15\text{mm}$ ($W_{fault}=4\text{mm}$), shown in Figure 3.14. Strong reflections were seen again from the generator side but not as large from the load side, and aperture localization was still obtainable. In each case, with both

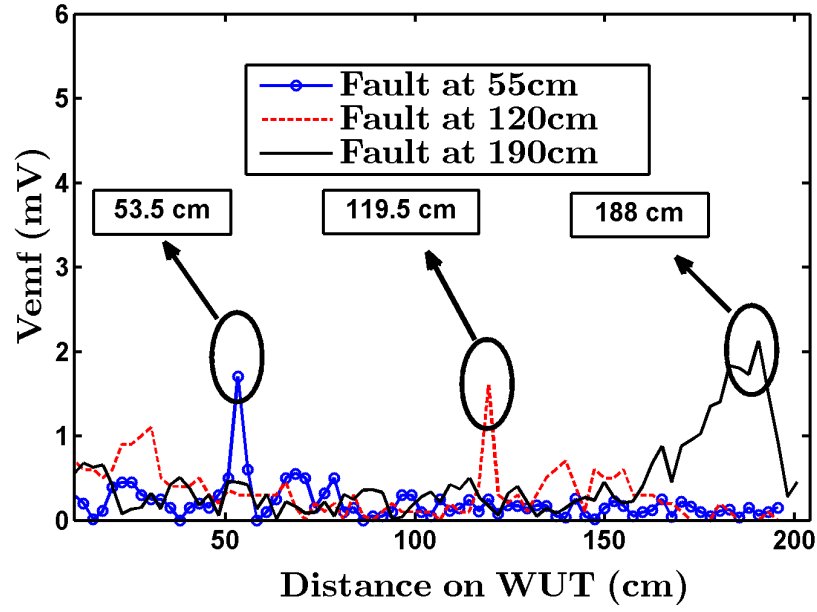


Figure 3.13: Measured V_{emf} from $L_{fault}=5\text{mm}$ long $W_{fault}=4\text{mm}$ wide fault.

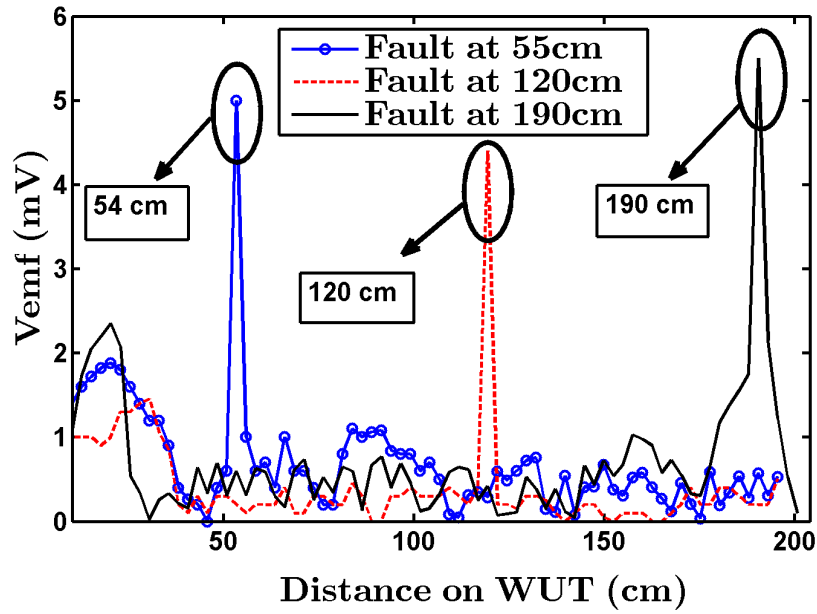


Figure 3.14: Measured V_{emf} from $L_{fault}=15\text{mm}$ long $W_{fault}=4\text{mm}$ wide fault.

a $L_{fault}=5\text{mm}$ long fault and a $L_{fault}=15\text{mm}$ long fault, $\pm 2\text{cm}$ accuracy was obtained in localization without additional signal processing. The worst case scenario was with a small fault, $L_{fault}=5\text{mm}$ long by $W_{fault}=4\text{mm}$ wide, when the fault was located close to the load end of the cable. Reflections from the load made localization difficult and less accurate. When the reflections from the load become strong and lower the signal to noise ratio, the fault waveform peaks are less sharp, as observed in Figures 3.13 and 3.14.

A novel method for localization of small apertures in cable shielding is described in this chapter. A signal is transmitted on the inside conductor of a shielded cable, where it leaks out of the damaged shield and is received on the outside of the cable. Through measurements and analysis, a ferrite loaded toroidal sensor was designed and tested for locating cable shield apertures. Several small faults $L_{fault}=5\text{-}15\text{mm}$ long and $W_{fault}=4\text{mm}$ wide on RG58 coax were localized, and the sensor performed as expected. The accuracy of the fault location with this particular sensor was $\pm 2\text{cm}$ on a two meter section of RG58.

The minimum damage that can be detected is dependent on the noise floor of the measurement equipment, environmental interference, and the distance of the fault from a load or source. The worst case scenario is having a very small fault, approximately $L_{fault}=1\text{mm}$ or smaller, and the fault being located near the end of the cable, within 10mm of a source or load. In that case, reflections from the load or source can dominate the reflection from the fault, and localization may not be as accurate.

Additional optimization could be done in the material selection of the sensor core to allow for optimal use at other frequencies. The optimization performed was done specifically for a test frequency of 200 MHz; however, this sensor can be designed for other applications and used at any frequency with the restriction of the material dispersion.

CHAPTER 4

COUPLING CROSSTALK IN MULTICONDUCTOR WIRING STRUCTURES

S/SSTDR is an emerging method for locating faults on wires and cables. Like other reflectometry methods, S/SSTDR sends a high frequency signal down the wire, where it reflects off of impedance discontinuities, including those associated with various types of faults. The reflected signal returns to the sending end of the wire, where it is received and analyzed. The time delay between the incident and reflected signal indicates the distance to the fault, and the nature of the reflected signal is associated with the type and magnitude of the fault. S/SSTDR uses a high frequency pseudo-noise (PN) code or sine wave modulated PN code as the test signal and a PN code correlator as the receiver [2]. PN codes have unique properties that they are highly uncorrelated with noise and other signals on the wires. This allows S/SSTDR to be used to locate intermittent faults on live wires without interfering with the existing signals and without being interfered with by them [3].

Testing live wires raises a very interesting question that is the topic of this paper. In many test applications where intermittent faults are of interest (in aircraft, for instance), it is common to find large bundles of adjacent, unshielded wires, all of which it may be desirable to test simultaneously. For example, under the aisle of a commercial aircraft it is common to have a wire tray that carries thousands of wires tightly bundled together, most of which are unshielded. Long, unshielded wires running close together in parallel provide coupling channels where high frequency signals can couple between them. This type of crosstalk coupling is typically analyzed in the signal integrity literature for all types of electronics, circuit boards, chips, etc. [6] [16]. It is also analyzed for aircraft during the design phase. Several parameters affect how much crosstalk is seen between adjacent lines: the proximity of the lines, their size/shape/configuration, materials the lines are made of, the nature of nearby lines, and the signals themselves. High frequency signals couple

more than low frequency signals. For our application and interest in reflectometry, this is very significant. It is possible and in fact likely that the wires under test were designed to carry lower frequency signals than the PN codes or other high frequency reflectometry signals. Thus, it is possible that the reflectometry signals will experience crosstalk when the original signals for which the wires are used do not. The ground or reference configuration (common grounds or not) also have a significant effect on the crosstalk, which will be discussed throughout this chapter.

This crosstalk may manifest itself in two ways. First, a signal used to test a single line (let's call this the aggressor line) may couple onto an adjacent line (the victim line). Reflections from impedance discontinuities on the victim line can then couple back onto the aggressor line, combining with reflections from impedance discontinuities on the aggressor line itself. Typically, when using reflectometry, we would only want to see the reflections from the impedance discontinuities on the aggressor line, so the reflections from the victim line will show up as unwanted noise in the reflectometry signature. This paper will explore the opportunity of utilizing those previously unwanted coupled reflections to help diagnose faults in adjacent lines from a single nearby aggressor line. While it will typically be difficult or impossible to determine exactly on which wire the fault occurs in that case, there are many applications where we may not care. For example, when wires are tightly bundled, the maintainer is going to have to access the entire bundle at the fault location in order to affect a repair. If the wire is in a bundle that is tightly wrapped, perhaps with a fabric or metallic braid, then it is likely the entire bundle would be replaced if a wire fault occurs any place in the bundle. Therefore, if we can test multiple wires with a single aggressor wire, we may be able to simplify reflectometry tests and embedded reflectometry test systems.

A second manifestation of crosstalk is seen when simultaneously testing adjacent wires. In practice, this is rarely if ever done with traditional reflectometry methods, but it is needed for S/SSTDR for continual monitoring for intermittent faults on live systems. Fortunately, PN codes used in S/SSTDR are highly uncorrelated with each other, depending on the types of codes used [2]. When multiple adjacent wires are tested simultaneously, the PN code on the aggressor wire may in fact couple onto a nearby victim wire. A second PN code is being used to test the victim wire, but its low cross correlation with the aggressor PN code will substantially reduce the interference caused by the two adjacent codes. This effect is quantified in Section 4.4 of this chapter.

The overall objective of this paper is to quantify and evaluate crosstalk and coupling of reflectometry signatures. We will focus on PN codes used in S/SSTDR. Section 4.4.1

will evaluate conditions when faults on adjacent lines are or are not seen on the aggressor line. These results are applicable to other reflectometry methods as well. Section 4.4.2 will quantify the level of cross coupling between orthogonal PN codes on adjacent wires. This is applicable mainly to S/SSTDR testing of live wires in bundles. These two evaluations provide a more complete understanding of the cross coupling that occurs when using reflectometry to test bundled wires, including both its challenges and opportunities.

4.1 Simulation Methods

To analyze the effects of coupling crosstalk on adjacent wires, a forward modeling method is needed to simulate both the signals on the aggressor wire and nearby victim wires. A forward model for a single transmission line, [16] [12], will be extended to multiple wires. In [16] [12], a 2D cross section of the wiring structure is simulated using the finite difference method (FDM) to calculate the transmission line parameters (*R-resistance*, *L-inductance*, *G-conductance*, *C-capacitance* per unit length). Single or multiple transmission lines with or without faults can be simulated. For the case of a multiconductor transmission line, the characteristic capacitance and inductance will be extracted as well as the coupling parameters, the mutual capacitance, and inductance. This will be described in Section 4.1. We will consider only lossless transmission lines in this paper, because it is slightly simpler and typically reflectometry signals are selected to be at frequencies where the lines are low loss to facilitate testing. As in [16] [12], these values are then entered into a finite-difference time domain (FDTD) simulator to obtain the reflectometry data from the entire system (described in Section 4.1.1) and perform any necessary postprocessing (described in Section 4.3) [2] [3]. S/SSTDR is evaluated after correlating the raw time domain PN code reflectometry signature from the FDTD simulation with the original excitation waveform [2] [3]. This correlated waveform, which we will now call the S/SSTDR signature, is then postprocessed to determine the corresponding time delay to the fault or other discontinuity and its nature. The end goal of the forward modeling method is to obtain the time domain reflectometry signature for analysis.

4.1.1 Finite Difference Time Domain (FDTD) for Coupled Lines

The characteristic equations that define how voltage and current behave on a transmission line in the time domain are the telegrapher's equations [12] [22].

$$\begin{aligned} -\frac{\partial v(z,t)}{\partial z} &= Ri(z,t) + L\frac{\partial i(z,t)}{\partial t} \\ -\frac{\partial i(z,t)}{\partial z} &= Gi(z,t) + C\frac{\partial v(z,t)}{\partial t} \end{aligned} \tag{4.1}$$

where R , L , G , C are the resistance, inductance, conductance, and capacitance per unit length, respectively, and V , I are voltage and current on the transmission line at location z (meters) and time t (seconds). A discrete form of these equations can be derived using a numerical central difference [17].

$$\begin{aligned} V_{k+1/2}^{n+1} &= c_1 \left(I_{k+1}^{n+1/2} - I_k^{n+1/2} \right) + c_2 V_{k+1/2}^n \\ I_k^{n+1/2} &= c_3 \left(V_{k+1/2}^n - V_{k-1/2}^n \right) + c_4 I_k^{n-1/2} \end{aligned} \quad (4.2)$$

The variables, c_{1-4} , are constants based on the spatial (k) and temporal resolution (n) of the simulation domain, and the RLGC parameters of the transmission line. The finite difference time domain (FDTD) method solves for V , I as a function of space and time. It is a versatile and robust simulation tool with a large variety of applications [24].

When multiple transmission lines are in proximity to one another, they share a mutual capacitance and inductance, shown by C_{12} and L_{12} in Figure 4.1, that need to be included in the FDTD simulation. The inductance and capacitance of a transmission line in this bundle of wires is now defined by both the characteristic parameters as well as the mutual parameters. These shared mutual parameters dictate how current and voltage couple from one line to an adjacent line.

The 1D telegrapher's equations account only for the characteristic RLGC parameters. With multiple lines, there are more parameters to consider. Figure 4.1 shows the lumped element schematic representation of a 3-conductor system, where one conductor acts as a common signal reference for the system. In this system, the inductance that defines transmission line 1 is a combination of its characteristic inductance (L_{11}) and its mutual inductance with transmission line 2 (L_{12}). The capacitance is analogous. In a healthy system where no faults are present, there will be no cross resistance or cross conductance terms. If one transmission line is subject to an open circuit fault, it will have a high load resistance term at that point. When a short circuit occurs between a conductor and its reference, the load conductance is low at that point. A cross conductance term would indicate a short circuit in the system between two nonreference conductors. For example, G_{12} would represent a short circuit between transmission line 1 and transmission line 2 and not between either transmission line and the common reference.

In order to account for these mutual impedance terms in the 1D telegrapher's equations, the RLGC coefficients become matrices rather than just scalar terms [7].

$$\mathbf{R} = \begin{bmatrix} R_{11} & R_{12} \\ R_{21} & R_{22} \end{bmatrix} \mathbf{L} = \begin{bmatrix} L_{11} & L_{12} \\ L_{21} & L_{22} \end{bmatrix} \mathbf{G} = \begin{bmatrix} G_{11} & G_{12} \\ G_{21} & G_{22} \end{bmatrix} \mathbf{C} = \begin{bmatrix} C_{11} & C_{12} \\ C_{21} & C_{22} \end{bmatrix} \quad (4.3)$$

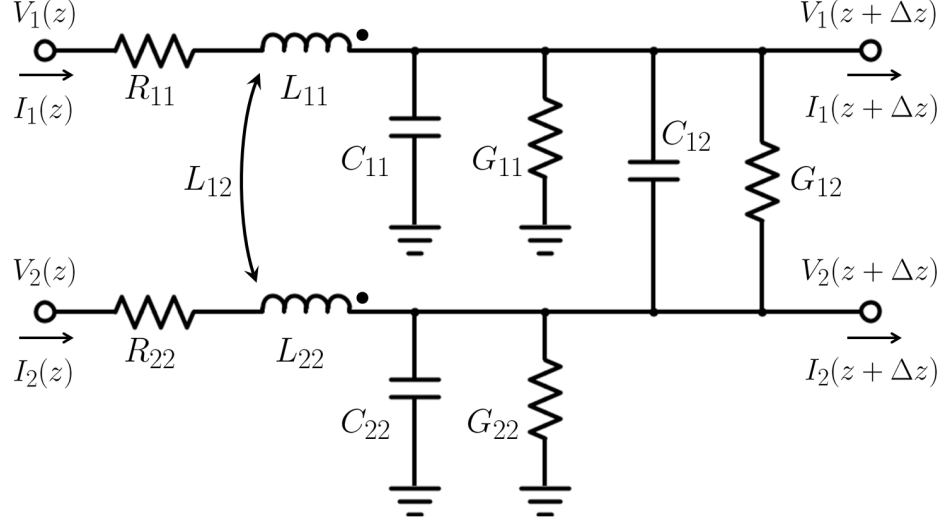


Figure 4.1: Circuit diagram of a multiconductor transmission line. This schematic represents two conductors that share a common reference conductor (a 3-wire or 3-conductor setup). This is a good example of two conductors that are using an airframe as their reference.

The diagonal elements will represent the RLGC values with respect to a central reference for the system and the off-diagonal elements represent the RLGC parameters between the two transmission lines. From Figure 4.1, L_{11} represents the characteristic inductance per unit length for transmission line 1 to ground whereas L_{12} and L_{21} will represent the inductive coupling between transmission line 1 and transmission line 2. The off-diagonal elements of the \mathbf{R} matrix should be zero at all times as no cross resistance terms should be defined. The off-diagonal elements of the conductance matrix, \mathbf{G} , can be used to represent a short circuit between two adjacent transmission lines, as well as defining the self-conductance term for a short circuit from a transmission line to ground, or a load. Then the telegrapher's equations become,

$$\begin{aligned} \mathbf{V}_{k+1/2}^{n+1} &= \mathbf{M}_1 \left(\mathbf{I}_{k+1}^{n+1/2} - \mathbf{I}_k^{n+1/2} \right) + \mathbf{M}_2 \mathbf{V}_{k+1/2}^n \\ \mathbf{I}_k^{n+1/2} &= \mathbf{M}_3 \left(\mathbf{V}_{k+1/2}^n - \mathbf{V}_{k-1/2}^n \right) + \mathbf{M}_4 \mathbf{I}_k^{n-1/2} \end{aligned} \quad (4.4)$$

where,

$$\begin{aligned} \mathbf{M}_1 &= -\frac{2\Delta t}{\Delta z} (2\mathbf{C} + \Delta t\mathbf{G})^{-1} \\ \mathbf{M}_2 &= (2\mathbf{C} + \Delta t\mathbf{G})^{-1} (2\mathbf{C} - \Delta t\mathbf{G}) \\ \mathbf{M}_3 &= -\frac{2\Delta t}{\Delta z} (2\mathbf{L} + \Delta t\mathbf{R})^{-1} \\ \mathbf{M}_4 &= (2\mathbf{L} + \Delta t\mathbf{R})^{-1} (2\mathbf{L} - \Delta t\mathbf{R}) \end{aligned} \quad (4.5)$$

4.1.1.1 Cross Conductance

When defining a cross conductance term to emulate a short circuit from transmission line 1 to transmission line 2, a correction must be made in order to accurately model the system. Since this system uses a central reference on the aggressor transmission line, indicated by the ground in Figure 4.1, a short circuit between the two victim lines has little meaning in the context of the reference. If a large self-conductance term is defined, G_{22} for example, this will indicate that there is a short circuit between the third line, the second victim wire, and the system reference. The terms to define a short circuit between the two victim lines are G_{12} and G_{21} . Both of these terms must be defined, and the self-conductance terms must also be modified to ensure power conservation and stability of the simulation. This can be better understood by examining Figure 4.1 and the voltage and current equations.

$$I_1(z+\Delta z) = I_1(z) + C_{11} \frac{\partial V_1(z+\Delta z)}{\partial t} + V_1(z+\Delta z)G_{11} + G_{12}[V_2(z+\Delta z) - V_1(z+\Delta z)] \quad (4.6)$$

The last term representing the differential conductance and differential voltage between the two lines must be added to the FDTD calculation. This is done modifying the conductance matrix to account for this extra voltage. To define a short circuit between the two victim lines, for instance, the cross conductance terms subtracted from the self conductance terms. Also note that the cross conductance terms are equal ($G_{12}=G_{21}$).

$$G'_{11} = G_{11} - G_{12} - G_{13} \quad (4.7)$$

This can be generalized for any of the self-conductance terms as:

$$G'_{ii} = G_{ii} - \sum_j G_{ij} (j \neq i) \quad (4.8)$$

This will ensure that the voltage and currents are being modeled correctly and that power within the system is conserved.

4.1.1.2 Time Step Criteria

Normally a transmission line has a set velocity of propagation (Vop) that can be calculated from the characteristic inductance and capacitance [22].

$$V_{op} = \sqrt{\frac{1}{LC}} \quad (4.9)$$

Since the inductance and capacitance are no longer scalar values but rather full matrices, the velocity of propagation is no longer quite as straightforward. For the 3-conductor line, including the reference, there are three velocities of propagation at which the signal may

travel: transmission line 1 to reference, transmission line 2 to reference, and transmission line 1 to transmission line 2. For the 1D FDTD algorithm, the stability criteria is based on the maximum velocity of propagation in the system: [16]

$$\Delta t \leq \frac{\Delta z}{V_{op}} \quad (4.10)$$

For a multiconductor transmission line, the velocity of propagation for each line is calculated by the eigenvalues (*eigs*) of the product of the inductance and capacitance matrices:

$$V_{op} = \text{abs} \left(\sqrt{\text{eigs}(\mathbf{LC})} \right)^{-1} \quad (4.11)$$

In order to satisfy the stability criteria for the time step, since there are multiple velocities of propagation in a multiconductor setup, the highest value of the calculated velocities of propagation was used in the calculation of the critical time step. This ensures stability over the entire simulation domain.

4.1.2 Finite Difference Method (FDM) Modeling

For calculating the transmission line parameters (RLGC), a finite difference method (FDM) solver was created for a cross section of an arbitrary wiring bundle structure, made up of any cylindrical shaped wire [12], [29]. The FDM is a powerful numerical tool that solves Poissons equation on a uniformly spaced 2D mesh grid (for this case of cross-sectional evaluation).

$$f'(x_o) = \frac{f(x_o + h) - f(x_o - h)}{2h} \quad (4.12)$$

This FDM simulation uses a central reference conductor for the mutual as well as self-inductance and capacitance parameters, as shown in the schematic in Figure 4.2 and field diagram in Figure 4.3. In this 4-wire setup, the self- and mutual-capacitance and inductance terms are calculated by exciting the nonreference wire with a positive voltage while exciting the reference conductor with an equal but opposite voltage. The boundary condition is set as a Dirichlet boundary of 0 volts on the outside of the region shown in Figure 4.3. FDM is then used to solve the Poisson equation,

$$\nabla^2 V(r) = -\frac{\rho(r)}{\epsilon_o \epsilon_r} \quad (4.13)$$

In order to get the charge on each wire, the electric field for the entire system is calculated from the voltage.

$$\overline{E}(r) = -\nabla V(r) \quad (4.14)$$

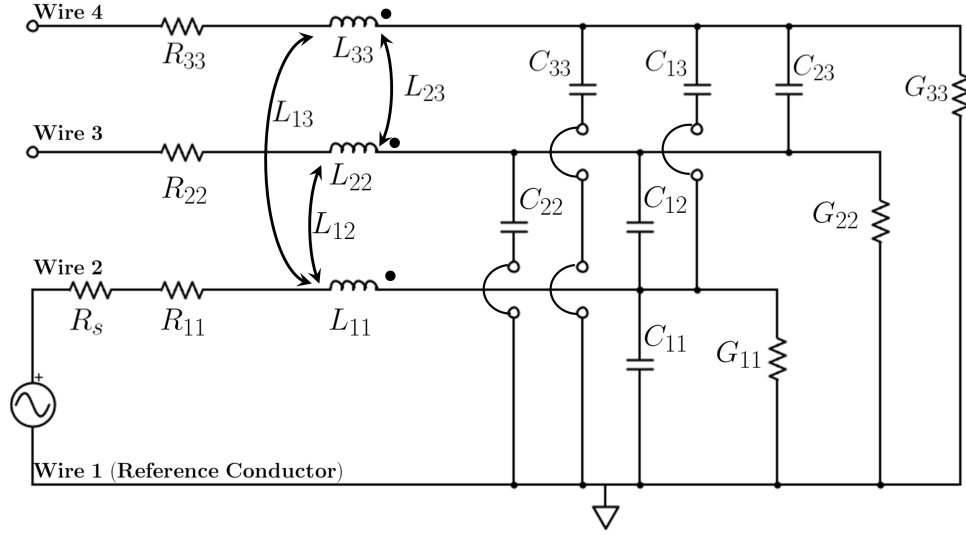


Figure 4.2: Circuit diagram of a multiconductor transmission line. This schematic represents 3 conductors that share a common reference conductor. This schematic represents a 4-wire ribbon cable that uses one of the outer conductors as the system reference.

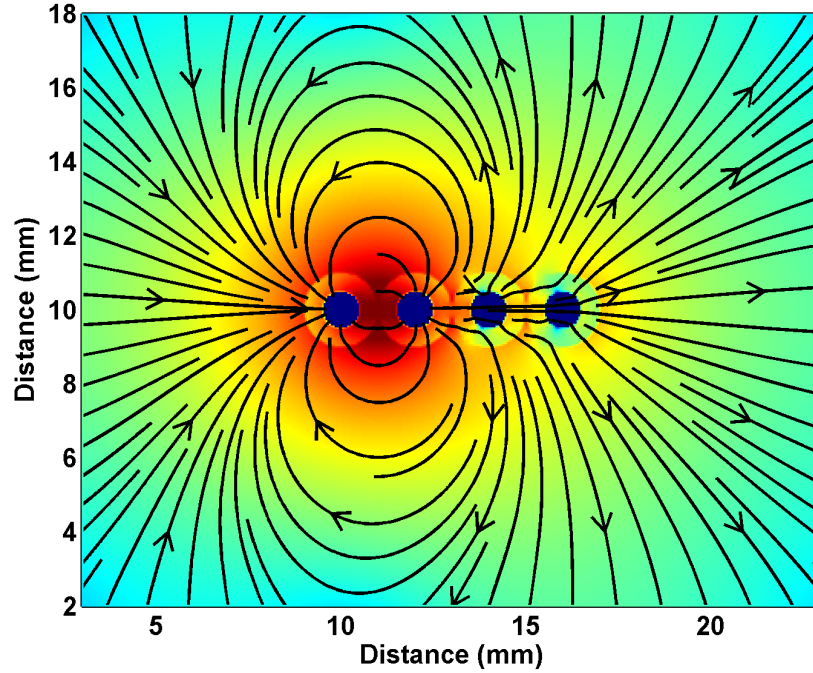


Figure 4.3: Electric field of a 4-wire ribbon cable due to an applied voltage from an aggressor wire. The color plot is in a logarithmic scale. From left to right: reference conductor, aggressor, victim 1, victim 2.

A Gaussian integral (Equation 4.15) is performed around the nonreference wires to determine the charge on the wire from the electric field coupling (Figure 4.3).

$$Q_j = \oint E_{field} dl \quad (4.15)$$

The integral will account for the charge on each wire induced by both the aggressor, second wire from the left in Figure 4.2, as well as other adjacent wires. The fields will couple from the aggressor to both victims, as well as the two victim wires influencing each other.

An intermediate term, called the **P** matrix, is introduced here. The **P** matrix is a square matrix of size $[N-1] \times [N-1]$, where N is the number of wires in the simulation including the reference for the system. the terms of the **P** matrix are given by the ratio of the excited voltage and the charge on the wire calculated by the Gaussian Integral (Equation 4.16).

$$\mathbf{P}_{ij} = \frac{V_i}{Q_j} \quad (4.16)$$

When there is only a single wire and the reference wire, a 2-wire transmission line, the **P** matrix is a single value, which is the self-capacitance and inductance of the transmission line. If the number of nonreference wires is two or greater, the **P** matrix is now holds multiple values. The capacitance is calculated as the inverse of the **P** matrix [16],

$$\mathbf{C}_{ij} = \mathbf{P}_{ij}^{-1} \quad (4.17)$$

while the inductance is calculated as the product of the P-matrix and the permittivity and permeability of free space.

$$\mathbf{L}_{ij} = \mu_o \epsilon_o \mathbf{P}_{ij} \quad (4.18)$$

The diagonal terms of the **L** and **C** matrices will represent the self-inductance and self-capacitance terms while the off-diagonal elements represent the mutual inductance and mutual capacitance terms. To correctly obtain the inductance matrix, the simulation must be run without dielectrics. To obtain the capacitance matrix, dielectrics must be included, as shown in Figure 4.4. This method can be executed to obtain the inductance and capacitance matrices for any N -conductor configuration by simply running the simulation $2(N-1)$ times. The inductance matrix and capacitance matrix each require $N-1$ runs. Each nonreference line in the simulation domain must be excited by a voltage individually and the charge on the adjacent wires calculated until the entire **P** matrix is full. A simulation was performed on a 4-wire ribbon cable with the specifications outlined in Table 4.1 and Figure 4.2. The results of the simulation, the capacitance, and inductance matrices are listed in Table 4.2 and Table 4.3. Once the coupling mechanisms have been calculated, the multiconductor

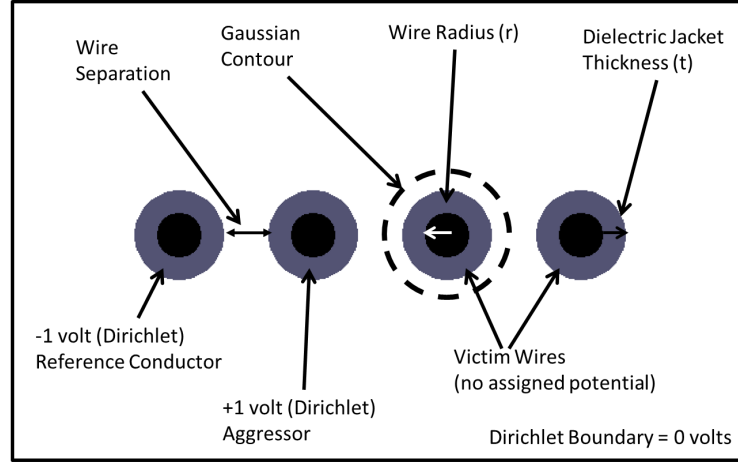


Figure 4.4: FDM system setup for a 4-wire ribbon cable. From left to right: reference conductor, aggressor, victim 1, and victim 2.

Table 4.1: Simulation parameters for 4-wire ribbon cable in Figure 4.4

Wire Radius	(r)	0.5 mm
Wire Separation	(D)	0.1 mm
Wire Length	(L)	4.0 mm
Dielectric Thickness	(t)	0.5 mm
Dielectric Constant	(ϵ_r)	3.5

Table 4.2: Inductance matrix of the 4-wire ribbon cable in Figure 4.4

0.51 $\mu\text{H/m}$	0.37 $\mu\text{H/m}$	0.32 $\mu\text{H/m}$
0.37 $\mu\text{H/m}$	0.74 $\mu\text{H/m}$	0.55 $\mu\text{H/m}$
0.32 $\mu\text{H/m}$	0.55 $\mu\text{H/m}$	0.87 $\mu\text{H/m}$

Table 4.3: Capacitance matrix of the 4-wire ribbon cable in Figure 4.4

104 pF/m	-45 pF/m	-4.8 pF/m
-47 pF/m	99 pF/m	-47 pF/m
-5.8 pF/m	-48 pF/m	60 pF/m

telegrapher's equation FDTD algorithm can be executed to determine the magnitude of the coupled signals based on the inductance and capacitance matrices calculated by the FDM solver.

4.1.3 Simulation Validation

A comparison was made using a square wave function generator to validate the FDTD and FDM simulation methods. The transmission line used in this test is defined from Table 4.1, a 4-wire ribbon cable comprised of 18 AWG lamp cord 4 meters in length. The inductance and capacitance matrices are shown in Table 4.2 and Table 4.3. The square wave generated measures two volts in amplitude, a 100ns rise time at a frequency of 2.5MHz. The signal was excited on the second wire while using the first wire as the reference conductor. The signal was then measured at the load end using capacitive probes and an Agilent Infiniium 54833A DSO oscilloscope. The voltage was measured on wires 2 and 3 (Figure 4.2) while using wire 1 as the reference conductor. A good agreement was found between the measured and simulated waveforms (Figure 4.5). Additional capacitance was inserted in series to the end of the line during simulation to account for the measurement probes and oscilloscope termination impedances.

This multiconductor FDTD algorithm is effective in simulating a time domain signal on a transmission line with multiple conductors to observe crosstalk coupling. The coupling parameters, the mutual capacitance and inductance, are accounted for in the algorithm by expanding the coefficients \mathbf{M}_{1-4} into matrices as well as the voltage and current into multidimensional arrays, rather than just a 1D scalar multiplication. In order to perform this simulation, the coupling parameters must be known. To quantify the coupling, the L_m and C_m parameters were calculated using a numerical solver.

4.2 Coupling Crosstalk

Crosstalk coupling from one transmission line to another is highly dependent on the geometry of the structure as well as the signal reference for each conductor. The separation distance between transmission lines can greatly affect the coupling/signal integrity as well as the placement of the reference point. There are two primary configurations that will be examined: a shared common reference between conductors (Figure 4.2) and an isolated reference configuration. The isolated reference will address two scenarios. The two situations investigated are simultaneous tests: 1) using the same PN code and frequency, and 2) using two different PN codes of the same length and frequency. For the common reference configuration, only one wire will be excited, as shown in Figure 4.2.

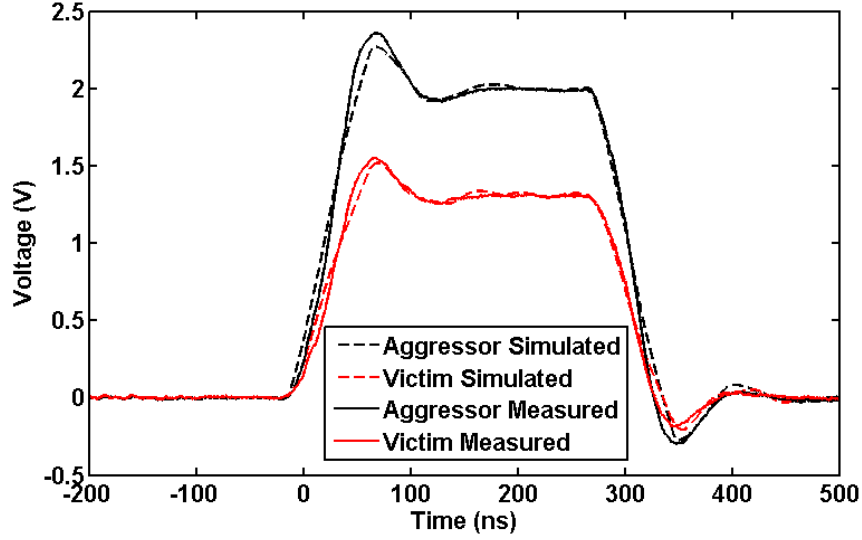


Figure 4.5: Square wave comparison using a multiconductor FDTD simulation on a 4-wire ribbon cable.

Each conductor must have a signal reference. A coaxial cable for example uses the outer conductor (shielding) as the reference. In aerospace, a possible reference point is the airframe. By using the airframe as the reference, each conductor shares a common signal reference and any two conductors in proximity to one another are approximately the same distance from that reference. The advantage in this configuration is that both wires will have very similar transmission line characteristics, specifically the velocity of propagation will be similar. Faults that appear in the waveform due to adjacent wires will still be in the vicinity of the observed fault. For this configuration, each wire will have separate characteristic RLGC values with respect to the reference (the diagonal terms in Table 4.2 and Table 4.3). They will also have a mutual capacitance and mutual inductance between each other, as in Figure 4.2 (the off-diagonal terms in Table 4.2 and Table 4.3). Under normal circumstances during testing in this configuration, each wire will have an open circuit impedance at the source and the load from the wire to reference since there is not a direct termination between a conductor and the airframe. When a reflectometry device is connected from a wire to reference, there will be some termination impedance at the source; however, the adjacent wires will still be open circuited. For this paper, the generator impedance termination used for these simulations (R_s in Figure 4.2) was matched to the transmission line impedance (Equation 4.19).

$$R_s = Z_{o11} = \sqrt{\frac{R_{11} + j\omega L_{11}}{G_{11} + j\omega C_{11}}} \Omega \quad (4.19)$$

The coupling parameters are dependent on the geometry and spacing of the wires. As the distance between the pair of wires (the aggressor and victim) and the reference conductor increases, the mutual coupling between the aggressor and victim increases and signal fidelity decreases. For this paper, the spacing of the wires in Figure 4.2 and Figure 4.4 was defined as $D=2.5\text{mm}$. This ensures some measure of signal fidelity as well as a separation distance that reasonably represents a real-life system. The faults simulated here are also hard faults.

For all the tests performed, the wire configuration used is a 4-wire ribbon cable described by Figure 4.4 and Table 4.1. All faults made are short circuits for visual ease of interpretation and distinguishing the fault from the end of the transmission line, which is modeled as an open circuit. The coupling crosstalk will be analyzed for several of the key faults that occur in this type of configuration:

- A short circuit between the aggressor wire and the system reference. A characteristic conductance term (G_{11}) is defined at a midpoint on the cable ($L=2.5\text{m}$). This will mimic very low impedance, or a short circuit, between the aggressor wire and the reference conductor for the system.
- A short circuit between a victim wire and the system reference. A characteristic conductance term (G_{22}) is defined at a midpoint on the cable ($L=2.5\text{m}$). Unlike the previous case, this line is not excited and also has an open circuit impedance at the generator side of the transmission line.
- A short circuit between the aggressor wire and a victim wire. Cross conductance terms G_{21} and G_{12} are defined at a midpoint on the cable ($L=2.5\text{m}$).
- A short circuit between the two victim wires. Cross conductance terms G_{23} and G_{32} are defined at a midpoint on the cable ($L=2.5\text{m}$). Unlike the first and third case, there is no native excitation to either wire.

The reference for these tests will be a wire within the bundled structure (see the caption for Figure 4.4). A qualitative analysis will be discussed on the difference between using a conductor within the bundle or a configuration more analogous to using the airframe as the system signal reference. The excitation used is an STDR signal. The length of the PN code is 31 bits. A longer code can be used; however, this will significantly increase the simulation time and any postprocessing required. The PN code was generated using a 200MHz clock rate. Soft faults are not addressed in the context of unshielded discrete wires.

4.2.1 Isolated Reference Testing

When testing wiring pairs separately, that is with no common reference to the 4 conductors, the coupling will behave in a manner very similar to that of a common reference

configuration (Figure 4.2). Figure 4.6 represents a configuration with no common signal reference to all the conductors in the system. Pair 1 contains two conductors where one acts as the reference for the other, while pair 2 has a separate reference from pair 1. However, since these measurements are being made differentially, any common mode signal on the pair under test is subtracted out of the measurement. As with the common reference configuration, pair 1 does have a native termination to pair 2 and the termination between the two (cross conductance terms) will appear as an open circuit. Each generator impedance (R_s) was matched to its respective transmission line characteristic impedance as with the common reference configuration.

For all the tests performed, the wire configuration used is a 4-wire ribbon cable described by Figure 4.4 and Table 4.1. All faults made are short circuits for visual ease of interpretation and distinguishing the fault from the end of the transmission line, which is modeled as an open circuit. The coupling crosstalk must be analyzed for the various fault situations that can be commonly seen in this configuration:

- A short circuit between an excited conductor and a nonnative reference wire. A short circuit will be placed at a midpoint on pair 1 ($L=2.5\text{m}$) between the excited wire of pair 1 and the excited wire of pair 2 by defining the cross conductance terms G_{21} and G_{12} . This fault will not be to any reference within the system, either on pair 1 or pair 2.

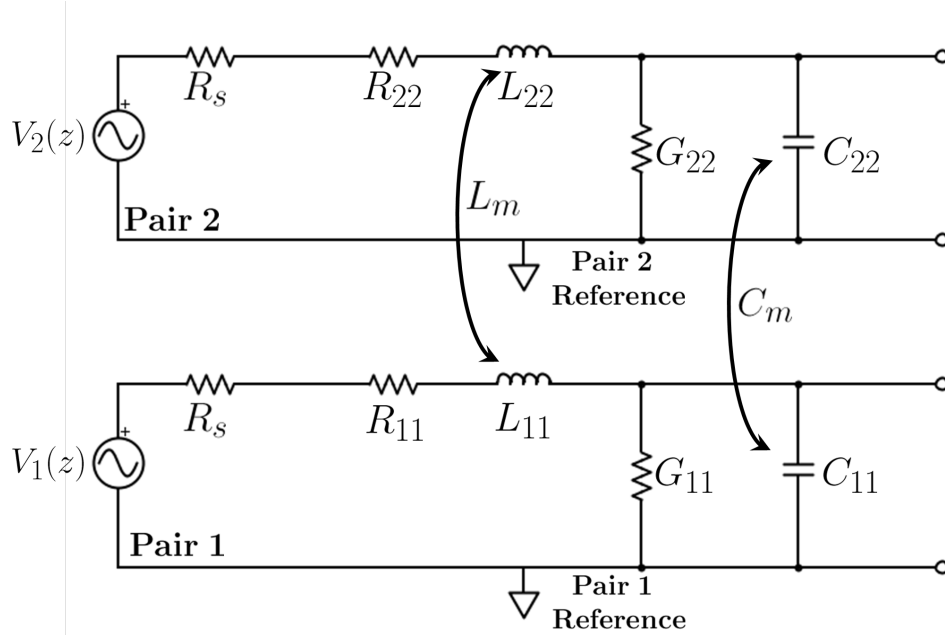


Figure 4.6: Circuit diagram of a multiconductor transmission line. This schematic represents a 4-conductor bundle with no common reference.

- A short circuit between an excited conductor and a nonnative reference wire. A short circuit will be placed at a midpoint on pair 1 ($L=2.5\text{m}$) between the excited wire of pair 1 and the excited wire of pair 2 by defining the cross conductance terms G_{21} and G_{12} . This fault will not be to any reference within the system, either on pair 1 or pair 2.

A qualitative analysis will also be discussed on the geometrical structure when testing in this configuration and how it pertains to testing a practical wiring bundle in the field. There is also a brief discussion on the difference between using different PN codes of the same length and using the exact same PN code for this method of testing. The excitation used is an STDR signal. The length of the PN code is 31 bits. A longer code can be used; however, this will significantly increase the simulation time and any postprocessing required. The PN code was generated using a 200MHz clock rate. Soft faults are not addressed in the context of unshielded discrete wires.

4.3 Analysis Methods

The test signal used in following section consists of the same STDR signal for all simulations. An unmodulated 31 bit PN code is generated at a 200MHz clock rate. A shorter code was necessary to keep simulation time low and to prevent instability in the simulation domain during the FDTD tests. To correctly model a cross conductance, there is a very small difference taking place in the voltage between the two conductors that are faulted. If the values are very small, this can lead to a numerical instability in the simulation. In order to analyze the output data from an STDR test, the waveform must be interpreted and the data understood. A fault on a transmission line has an associated magnitude and phase with its reflection coefficient. That coefficient is determined by the characteristic impedance of the transmission line under test and the impedance of the fault.

$$\Gamma = \frac{Z_L - Z_o}{Z_L + Z_o} \quad (4.20)$$

If a short circuit is present, the load impedance goes to $Z_L=0$ and the resulting reflection will be $\Gamma=-1$. If an open circuit is present on the transmission line, an ideal open circuit load impedance would approach $Z_L=\infty$ and the resulting reflection is $\Gamma=+1$. As a side note, it can be shown that the magnitude of a real valued characteristic impedance terminated by a complex valued load is $|\Gamma|=1$. These reflection coefficients are a scaling factor of the incident voltage. Since the generator impedance, R_s from Figure 4.2, is matched to the transmission line, there is a 1:1 voltage divider. The incident voltage into the transmission line is 1 volt so the maximum reflection magnitude from an ideal short or open circuit that

should be observed is $V_1 \cdot |\Gamma| \approx 0.5$. To better understand this, Figure 4.7 shows the three common cases. When no fault is present, the only observed waveform shape is the initial correlation lobe at the beginning of the transmission line (blue solid line in Figure 4.7). The magnitude of this lobe, $\rho \approx 0.5$, is expected with the match generator impedance to the transmission line. For the case of a short circuit at two meters (red dashed line in Figure 4.7), the correlation value is $\rho \approx -0.5$. As with the short circuit case described above, this is the expected value for a short circuit on a transmission line. This will be the fault signature for all of the faults present in the simulations for this thesis. For the case of the open circuit (magenta line with circles in Figure 4.7), the correlation value is $\rho \approx +0.5$. This will be the end of line signature for all simulation waveforms since the load impedance for these multiconductor transmission lines are modeled as open circuits.

4.3.1 Time Domain Derivatives

Coupling from one transmission line to another in effect high pass filters a signal. A high pass filter is similar to differentiating a signal in the time domain. Since the STDR signal is coupling from one line to another, the derivatives of the correlation should also

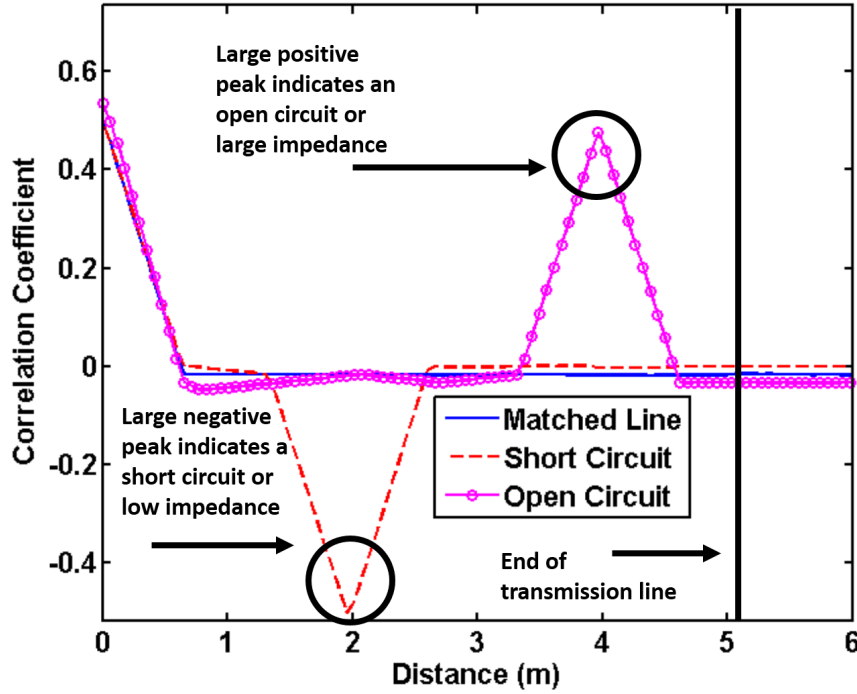


Figure 4.7: An STDR response for a transmission line for 3 common cases: a matched line with no fault, a short circuit, and an open circuit.

be present in the STDR waveform. The presence of these anomalies could indicate a fault on an adjacent wire. A test signal will propagate down a transmission line, reflecting off a discontinuity. This reflection can then couple to an adjacent line. When correlating this coupled signal with the original test signal, the derivative of the STDR fault signature will be present. Figure 4.8 shows the correlation signature of a standard STDR waveform shape. Figure 4.8 also shows the result of correlating with the first and second derivative in time respectively. The magnitude of the derivative is several orders of magnitude smaller than the desired fault response. Even if these waveform anomalies are present and observable, due to their magnitude in comparison with an ideal fault signature, their presence should not interfere with the ability to locate a fault. If the intent is to identify these first and second derivative anomalies, their minute magnitude will be an issue if the signal has a large variance.

4.3.2 Standard Deviation of Noise Floor

One method of detecting a fault is to simply look beyond $\pm n$ standard deviations ($\pm n\sigma$) of the noise floor in the correlation waveform where n is a scalar value. The correlation

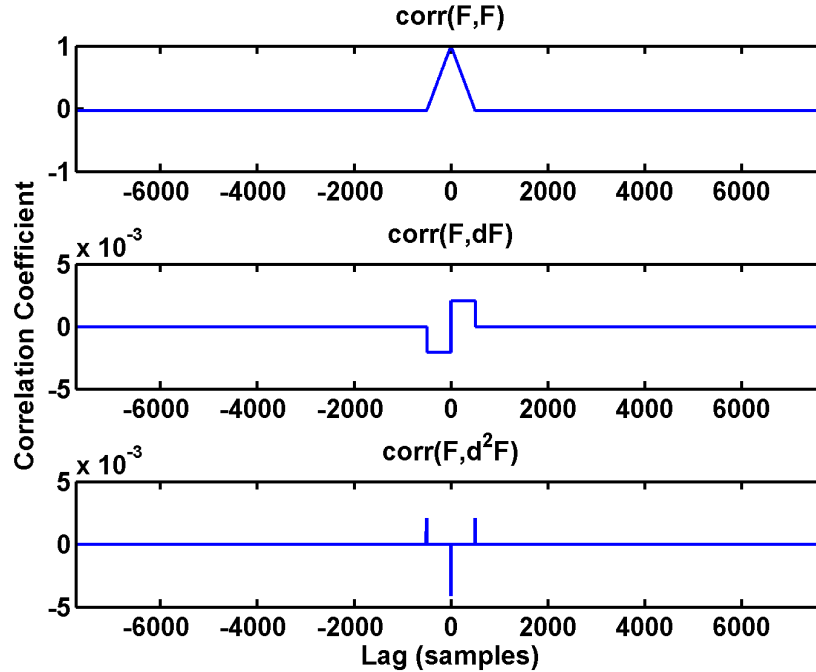


Figure 4.8: The correlation signatures of a 7-bit STDR sequence with itself, $\text{corr}(F,F)$, (top), its first derivative in time, $\text{corr}(F, \frac{\partial F}{\partial t})$, (middle) and its second derivative in time, $\text{corr}(F, \frac{\partial^2 F}{\partial t^2})$, (bottom).

coefficient, $\rho = \left(\frac{-1}{N}\right)$, should be small in the absence of a fault or coupling crosstalk interference. Since this paper is focused on hard faults (short circuits and open circuits where the reflection coefficient is ideally $\Gamma \pm 1$), simply picking a large threshold beyond $\rho = \left(\frac{-1}{N}\right)$ should isolate hard fault signatures while dismissing false faults.

To determine this threshold, a baseline configuration was simulated based on the parameters in Table 4.1 and Figure 4.2 with no faults present in the system. The load ends of each conductor were assigned a high impedance (open circuit). An STDR test signal was injected on wire 2 and measured on wire 1, wire 2, and wire 3. These recorded time domain data were correlated with the original test signal. The standard deviation was calculated from the correlated data on the aggressing wire, wire 1. The output for this simulation is shown in Figure 4.9.

The end of the transmission line is visible on all wires in the bundle. There is also a small anomaly in the middle of the waveform near 2.5 meters on the second victim wire as well as the end of both victim transmission lines. The open circuit signature at the end of the transmission line has as anomaly near the end of the transmission line at 5.5 meters. This negative lobe protruding beyond σ is due to the first derivative effect; however, it is distorted and not of a square wave shape (Figure 4.8). As the transmission line is extended

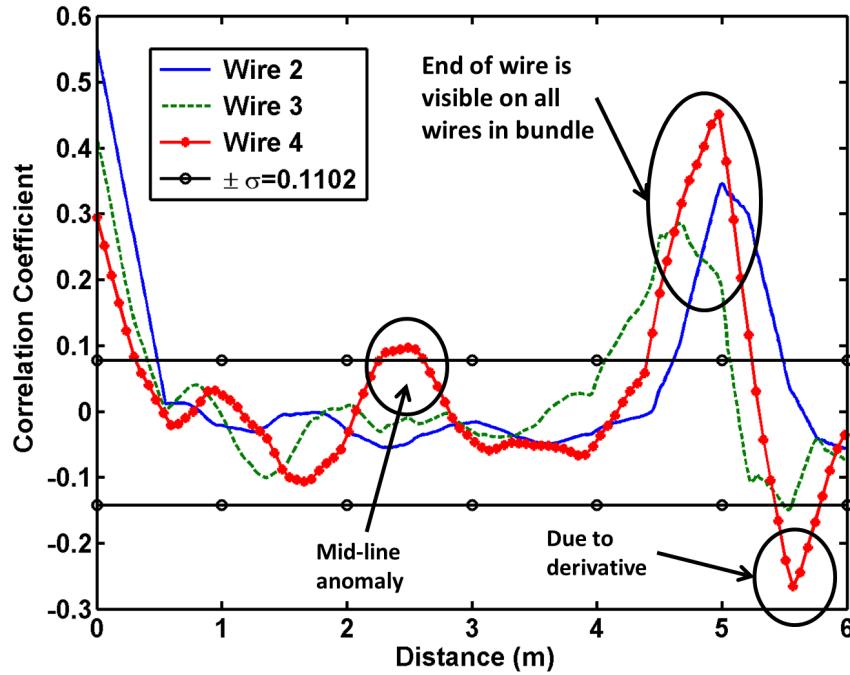


Figure 4.9: A multiconductor FDTD simulation output of a STDR test performed on the 4-wire ribbon cable described by Table 4.1 and Figure 4.2.

in length and the distance between the point of excitation and the first observable fault increases, the victim waveform variance decreases and the midline anomaly magnitude will shrink below the threshold. As this distance between the source and load increases, the first derivative shape at the end of the victim wires will begin to take on a cleaner first derivative shape in Figure 4.8 rather than the distorted shape seen in Figure 4.9. The threshold for determining the location of faults for this thesis is $\pm\sigma$.

4.4 Results

Two configurations were examined: 1) a common reference configuration, illustrated in Figure 4.2, and 2) an isolated reference configuration, illustrated in Figure 4.6. Several cases are presented for the common reference configuration to illustrate and quantify the effects of coupling crosstalk in STDR testing on unshielded discrete wire bundles.

4.4.1 Common Reference Configuration

For the common reference case, 4 scenarios were investigated: 1) an aggressor to reference fault, 2) a victim to reference fault, 3) an aggressor to victim fault, and 4) a victim to victim fault. The results for each test are illustrated in the following sections. In each case, there are 3 waveforms. The signal is applied to the aggressor wire, wire 2 in Figure 4.2. The STDR waveform for this wire appears as a blue solid line in each plot. The first victim wire, wire 3, appears as a green dashed line and the second victim wire, wire 4, is a red line with asterisks (*). A black horizontal line with circles marks $\pm\sigma$ for each waveform. The standard deviation was calculated from the aggressor wire, wire 2, only.

4.4.1.1 Aggressor to Reference Fault

The first case examined is when there is a short circuit from the aggressor wire to the reference conductor at 2.5 meters. When a short circuit occurs on a transmission line, the signal should reflect off the fault entirely. For an ideal short circuit, 0% of the signal will be transmitted through the fault. The aggressor wire, the faulted wire, waveform in Figure 4.10 supports this idea. There is some slight variation in the waveform near the end of the transmission line. This is due to crosstalk coupling and reflections from adjacent wires. The two victim wires also exhibit the first derivative shape at the end of the transmission line. As with the matched case, if the transmission line length and the distance from the fault to the end of the lines is increased, this shape becomes more idealized, as shown in Figure 4.8. Notice that the actual fault is visible beyond the threshold ($\pm\sigma$) on all wires within the bundle; however, it is largest ($\rho=-0.46$) on the aggressor wire, wire 2, which is where the

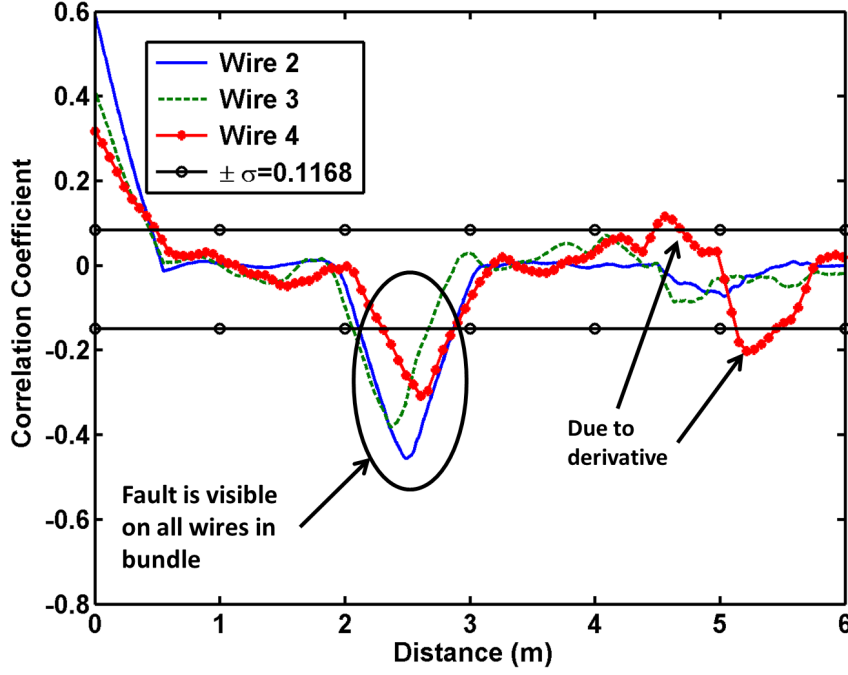


Figure 4.10: STDR signatures from the 4-wire ribbon cable detailed in Figure 4.4 and Table 4.1 when a short circuit ($G_{11} \gg 1$) is defined between wire 2 and the reference conductor in Figure 4.2.

fault occurs. The distance of the fault is correct on the aggressor wire, while it is shifted spatially on the victim wires. This is due in part to the signal traveling at a different VOP on the victim wires than the aggressor wire, and also due to crosstalk coupling causing a superposition of STDR signatures. Similar results are seen in the case of an open circuit on the aggressor wire. The fault is visible on each wire within the bundle; however, the fault signature on the victim wires is inverted from the fault signature on the aggressor wire. The variance in this case is similar. For a short circuit $\sigma=0.1168$, and for an open circuit $\sigma=0.1126$.

4.4.1.2 Victim to Reference Fault

The second case investigated was the case of a short circuit fault on a victim wire to the reference conductor at 2.5 meters. When this fault occurs, it is easily visible on all wires within the bundle beyond the threshold ($\pm\sigma$) as is the end of the transmission line, shown in Figure 4.11. The smallest fault signature ($\rho=-0.21$) at the fault location (2.5 meters) is seen on the aggressor wire and is twice the threshold of $\sigma=-0.1067$. As with the previous case of a fault on the aggressor wire to the reference conductor, the largest signature ($\rho=-0.61$) is

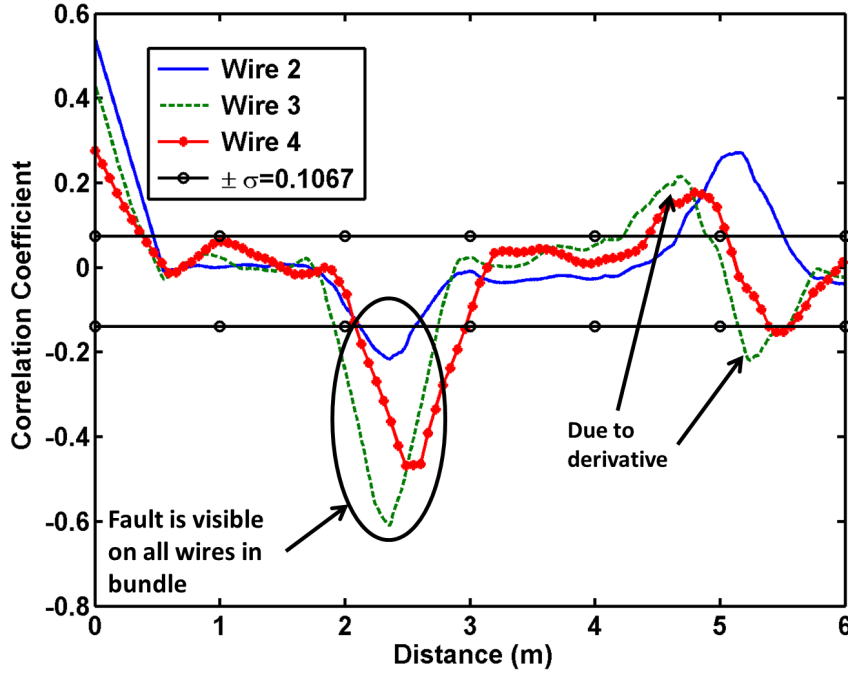


Figure 4.11: STDR signatures from the 4-wire ribbon cable detailed in Figure 4.4 and Table 4.1 when a short circuit ($G_{22} \gg 1$) is defined between wire 3 and the reference conductor in Figure 4.2.

visible on the wire that is faulted, wire 3. If an open circuit occurs on a victim wire, wire 3, the fault is not visible on the aggressor wire, wire 2, or the faulted wire, wire 3. There is a perturbation ($\rho = +0.1167$) on wire 4 that exceeds the threshold of $\sigma = +0.1107$. While this lobe is barely over the threshold, it is visible.

4.4.1.3 Aggressor to Victim Fault

The third case that was analyzed is the occurrence of a fault between the aggressor wire and a victim wire at 2.5 meters, a short circuit between wire 2 and wire 3 in Figure 4.2. The end of the bundle is visible on all wires as was the case when no fault was present on the aggressor wire, shown in Figure 4.12. In this situation, the fault is visible on both victim wires but not the aggressor wire. This case also has the smallest standard deviation as compared with the case of a fault occurring between a wire and the system reference conductor. The fault signature present on the victim wires is also inverted. While wire 3 appears to be a normal signature shape, the waveform shape of the fault signature on wire 4 has similar properties to the derivative correlation of an STDR waveform (Figure 4.8). The largest signature present on the bundle ($\rho = +0.40$) is on wire 4 where no fault is

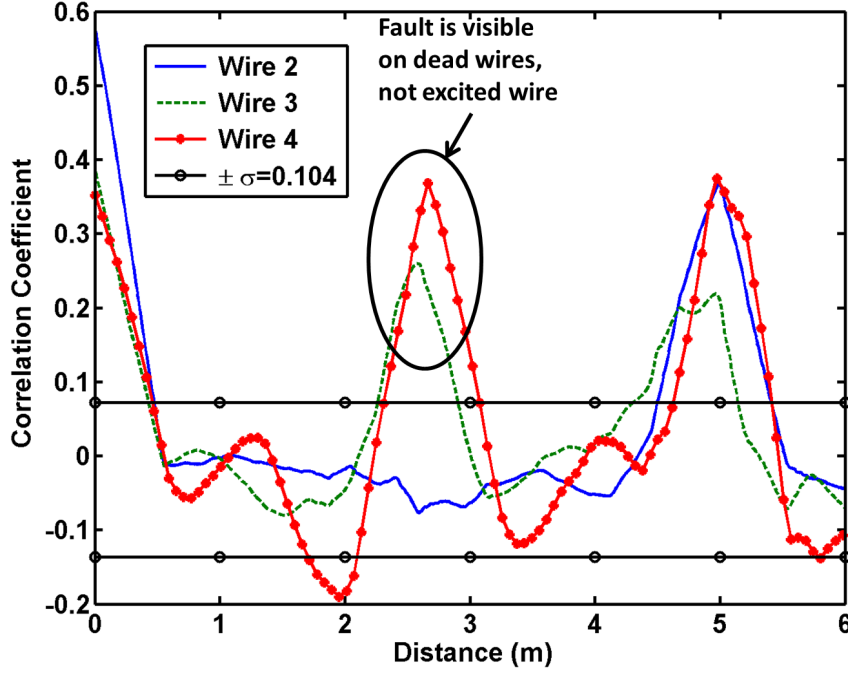


Figure 4.12: STDR signatures from the 4-wire ribbon cable detailed in Figure 4.4 and Table 4.1 when a short circuit ($G_{21} \gg 1$) is defined between wire 2 and wire 3 in Figure 4.2.

present. The fault signature is present on wire 3 ($\rho = +0.29$) where the fault occurs. There is also a false peak ($\rho = -0.19$) at 1.95 meters, where no fault is present. This level is beyond the threshold and can give a false reading. In this case, using a larger threshold ($\pm 1.5\sigma$) is desired. For this scenario, simply recording the data from the aggressor wire is insufficient to detect a fault. The data from each wire within the bundle are required. The open circuit case was not considered for this configuration as a cross resistance term holds no meaning. An open circuit cannot occur between two adjacent conductors.

4.4.1.4 Victim to Victim Fault

The fourth and final case considered for this reference configuration is a cross fault between two victim wires at 2.5 meters, a short circuit between wire 3 and wire 4 in Figure 4.2. For this situation, there is no excitation native to either faulted wire. Similar to the cross fault case in Section 4.4.1.3, the end of the transmission lines are visible on all wires within the bundle when no fault is present on the aggressor wire, shown in Figure 4.13. This fault is not visible on the aggressor wire, wire 2, where there is no fault, or on the first victim wire, wire 3, where the fault occurs. The standard deviation ($\sigma = 0.1048$) is

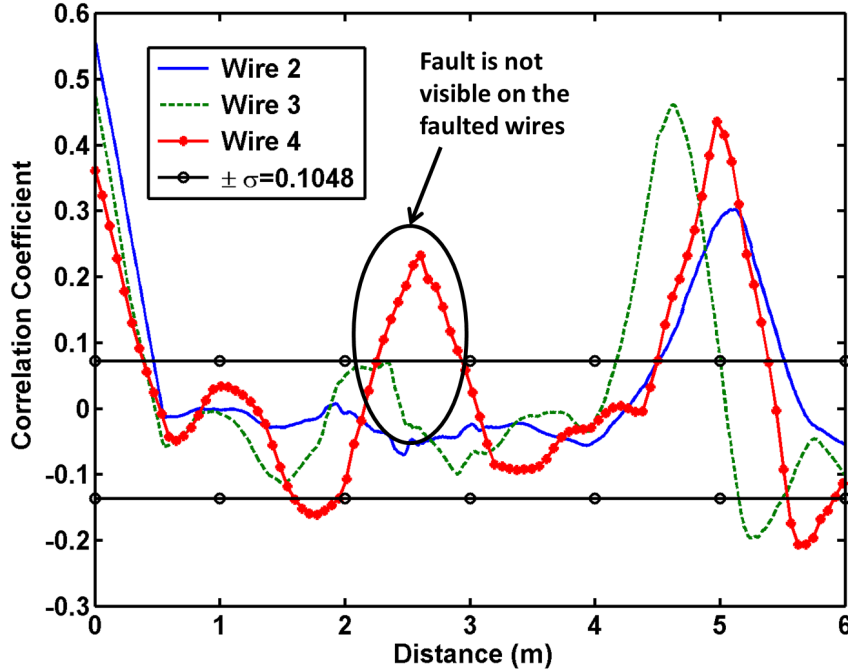


Figure 4.13: STDR signatures from the 4-wire ribbon cable detailed in Figure 4.4 and Table 4.1 when a short circuit ($G_{32} \gg 1$) is defined between wire 3 and wire 4 in Figure 4.2.

also smaller than when a fault occurs between a wire and the system reference conductor. The lower threshold allows a false peak ($\rho = -0.16$) to occur at 1.7 meters. There is no fault in the system at this location. This level is beyond the threshold and can give a false reading. In this case, using a larger threshold ($\pm 1.5\sigma$) is desired. For this scenario, simply recording the data from the aggressor wire is insufficient to detect a fault. The data from each wire within the bundle are required. The open circuit case was not considered for this configuration as a cross resistance term holds no meaning. An open circuit cannot occur between two adjacent conductors.

4.4.2 Isolated Reference Configuration

For the isolated reference configuration shown in Figure 4.6, two cases were investigated: 1) a short circuit on pair 1 while pair 2 is not faulted and 2) a cross fault between pair 1 and pair 2. The cross fault is a short circuit between an excited conductor and a nonreference conductor. The signal applied to each pair is an STDR test signal of the same PN code length (31 bit) and frequency (200 MHz); however, the PN codes are different. The STDR waveform for pair 1 appears as a blue solid line in each plot while pair 2 appears as a red

dashed line. As with the common reference configuration, the black horizontal line with circles represents the fault detection threshold ($\pm\sigma$). The threshold was calculated as the standard deviation of the correlation waveform from pair 1.

4.4.2.1 Excited Conductor to Reference Conductor Fault

For the case of a fault between an excited conductor and its reference, a short circuit was assigned to pair 1 at 2.5 meters. The fault is easily detectable on pair 1, while only the end of the transmission line is detectable on pair 2, shown in Figure 4.14. In this case, the common signal to both conductors in pair 2, the coupled signal from pair 1, is subtracted out and does not interfere with the ability to detect the end of the transmission line, and similarly, the coupled signal from pair 2 does not hinder the ability to detect the short circuit present on pair 1. For the case of an open circuit, the results are similar; however, due to coupling crosstalk, the end of the transmission line is visible on the faulted pair. In this configuration, the crosstalk is not detrimental to fault detection using STDR.

4.4.2.2 Excited Conductor to Nonreference Conductor Fault

For the case of a fault between an excited conductor and a nonreference conductor, a cross conductance short circuit was assigned between pair 1 and pair 2 at 2.5 meters. In this case, the threshold ($\sigma = .1607$) increases significantly from the previous case ($\sigma = .1065$) of no cross faults present in the system. The end of the transmission line is visible on both pairs well beyond the threshold as was the case in the common reference configuration when no faults occurred between an excited conductor and its reference conductor. In this case, there is a short circuit in the system at 2.5 meters; however, the fault is not visible on either pair, shown in Figure 4.15. At the fault location, 2.5 meters, there is a waveform shape similar to the second derivative (Figure 4.8); however, this is below the threshold and will not be detected. In this case, the fault that is present in the system cannot be detected using this testing method.

This chapter has investigated the use of STDR for testing multiconductor wiring structures using a common reference to all conductors as well as using an isolated reference for each conductor. When using a common reference to all conductors, the waveforms from all wires in the bundle must be considered. For the case of a cross fault between an aggressor wire and a victim wire, or a cross fault between two victim wires, the fault is not visible on the aggressor wire and can be overlooked. Also in both of these cases, the standard deviation ($\sigma=0.104$) was lower than the other case of a hard fault to the reference conductor ($\sigma=0.107$ and 0.117). This lower threshold introduced false faults in the waveform. This cross fault

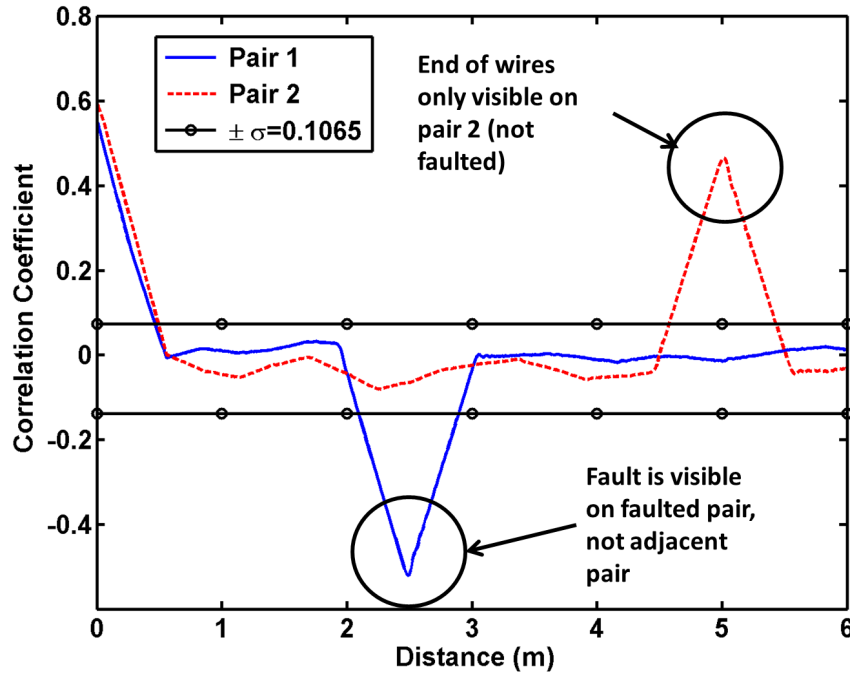


Figure 4.14: STDR signatures from the 4-wire ribbon cable detailed in Figure 4.4 and Table 4.1 when a short circuit ($G_{11} \gg 1$) is defined on pair 1 from Figure 4.6.

case is a worst case scenario. For the situation of using an isolated reference, the coupling crosstalk is not sufficient to interfere with fault detection when a fault occurs between an excited conductor and its reference, short circuit or open circuit. As with the common reference case, the worst case scenario is when a cross fault occurs. This fault is not visible on either conductor and will be overlooked in testing. In all cases, when a fault is not present between the excited conductor and its reference conductor, the end of the transmission line is visible.

In order to accurately detect faults on multiconductor wiring structures, both testing methods must be considered. A fault between a conductor and its reference conductor is easily detectable. A cross fault is not. For cross fault consideration, the only method to detect it is using a common reference and analyzing the data on adjacent lines.

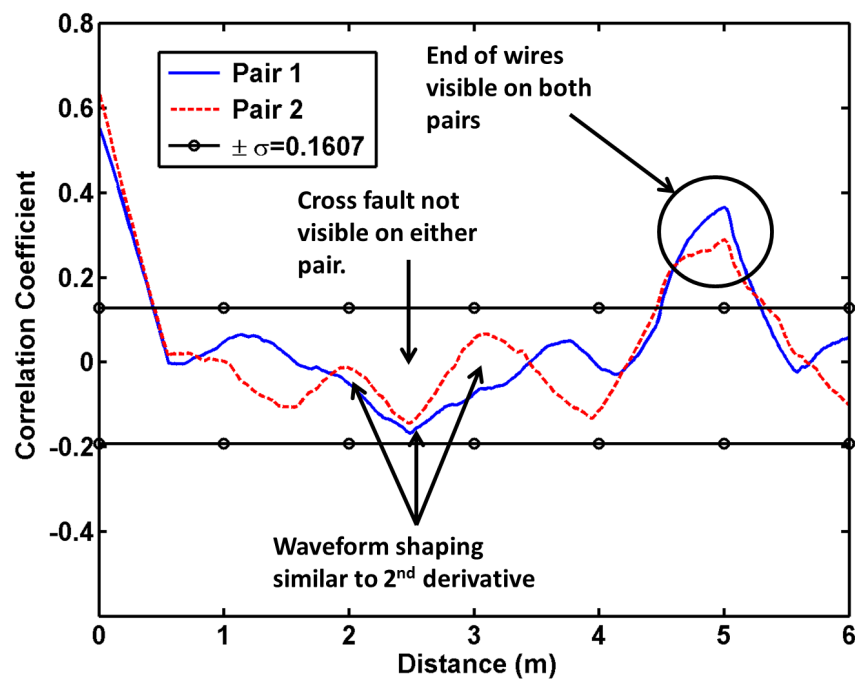


Figure 4.15: STDR signatures from the 4-wire ribbon cable detailed in Figure 4.4 and Table 4.1 when a cross conductance short circuit is defined from pair 1 to pair 2 from Figure 4.6.

CHAPTER 5

CONCLUSION

The contributions of this thesis are a novel approach for locating coaxial cable shield apertures and an in depth investigation of coupling crosstalk on unshielded discrete wire transmission lines using S/SSTD. This thesis has presented a new method for locating small apertures in coaxial cable shielding using a ferrite loaded toroidal sensor. This work has included a characterization of the frequency response of the apertures as well as the characterization and design of the toroidal sensor used for aperture localization. This work has also investigated coupling crosstalk in S/SSTD for discrete wiring structures for two separate reference configurations: 1) using a common reference for multiconductor bundles and 2) simultaneous testing of multiple pair transmission lines using an isolated reference. The effects of coupling crosstalk were analyzed and quantified to determine the validity of testing with these methods.

5.1 Summary of Aperture Coupling

A novel method for localization of small apertures in cable shielding is described in this thesis. When a small hole in cable shielding occurs, electromagnetic fields can leak from the fault. A signal is transmitted on the inside conductor of a shielded cable, where it leaks out of the damaged shield and is received on the outside of the cable. Frays acting as these small holes, which have a poor low frequency response and a stronger response at high frequencies, act like high pass filters, where only high frequencies are coupled onto the outside of the cable. This, in effect, differentiates the original signal that was on the inside of the cable.

Through measurements and analysis, a ferrite loaded toroidal sensor was designed and tested for locating cable shield apertures. Several small faults $L_{fault} = 5-15\text{mm}$ long and $W_{fault} = 4\text{mm}$ wide on RG58 coax were localized, and the sensor performed as expected. The accuracy of the fault location with this particular sensor was $\pm 2\text{cm}$ on a two meter section of RG58.

The minimum damage that can be detected is dependent on the noise floor of the measurement equipment, environmental interference, and the distance of the fault from a load or source. The worst case scenario is having a very small fault, approximately $L_{fault}=1\text{mm}$ or smaller, and the fault being located near the end of the cable, within 10mm of a source or load. In that case, reflections from the load or source can dominate the reflection from the fault, and localization may not be as accurate.

Additional optimization could be done in the material selection of the sensor core to allow for optimal use at other frequencies. The optimization performed was done specifically for a test frequency of 200 MHz; however, this sensor can be designed for other applications and used at any frequency with the restriction of the material dispersion.

5.2 Summary of Wire to Wire Coupling

When using a common reference to all conductors, the waveforms from all wires in the bundle must be considered. For the case of a cross fault between an aggressor wire and a victim wire, or a cross fault between two victim wires, the fault is not visible on the aggressor wire and can be overlooked. Also in both of these cases, the standard deviation ($\sigma=0.104$) was lower than the other case of a hard fault to the reference conductor ($\sigma=0.107$ and 0.117). This lower threshold introduced false faults in the waveform. This cross fault case is a worst case scenario. For the situation of using an isolated reference, the coupling crosstalk is not sufficient to interfere with fault detection when a fault occurs between an excited conductor and its reference, short circuit or open circuit. As with the common reference case, the worst case scenario is when a cross fault occurs. This fault is not visible on either conductor and will be overlooked in testing. In all cases, when a fault is not present between the excited conductor and its reference conductor, the end of the transmission line is visible.

In order to accurately detect faults on multiconductor wiring structures, both testing methods must be considered. A fault between a conductor and its reference conductor is easily detectable. A cross fault is not. For cross fault consideration, the only method to detect it is using a common reference and analyzing the data on adjacent lines.

5.3 Final Thoughts

Previous research has traditionally used reflectometry only in controlled impedance situations for accurate fault detection while uncontrolled impedance cables are often overlooked. The work in this thesis contributes to understanding how the coupling of S/SSTD signals affects fault detection for several situations: localizing coaxial cable shield apertures, and

coupling crosstalk between discrete wiring structures. Further research is warranted in the area of discrete unshielded cables to determine more efficient methods for detecting a cross fault.

REFERENCES

- [1] C. Furse and R. Haupt, "Down to the wire [aircraft wiring]," *Spectrum, IEEE*, vol. 38, no. 2, pp. 34-39, Feb 2001.
- [2] P. Smith, C. Furse, and J. Gunther, "Analysis of spread spectrum time domain reflectometry for wire fault location," *Sensors Journal, IEEE*, vol. 5, no. 6, pp. 1469-1478, 2005.
- [3] C. Furse, P. Smith, M. Safavi, and Chet Lo, "Feasibility of spread spectrum sensors for location of arcs on live wires," *Sensors Journal, IEEE*, vol. 5, no. 6, pp. 1445-1450, Dec 2005.
- [4] L.A. Griffiths, R. Parakh, C. Furse, B. Baker, "The invisible fray: a critical analysis of the use of reflectometry for fray location," *Sensors Journal, IEEE*, vol.6, no.3, pp.697-706, June 2006.
- [5] D. Lee and P. Arnason, "U.S. Navy wiring systems lessons learned," in *Joint Conference on Aging Aircraft*, May 2000.
- [6] E. Bogatin, *Signal Integrity - Simplified*. Upper Saddle River, NJ: Prentice Hall, 2004.
- [7] C. R. Paul, "Computation of Crosstalk in a Multiconductor Transmission Line," *Electromagnetic Compatibility, IEEE Transactions on*, vol. EMC-23, no. 4, pp. 352-358, Nov 1981.
- [8] C. S. Walker, *Capacitance, Inductance and Crosstalk Analysis*. Norwood, MA: Artech House, Inc., 1990.
- [9] C. Furse, Y. C. Chung, C. Lo, and P. Pendayala, "A critical comparison of reflectometry methods for location of wiring faults," *Smart Structures and Systems*, vol. 2, no. 1, pp. 25-46, 2006.
- [10] C. Furse, P. Smith, and M. Diamond, "Feasibility of Reflectometry for Non-destructive Evaluation of Prestressed Concrete Anchors," *IEEE Sensors Journal*, vol. 9, no. 11, pp. 1322-1329, Nov 2009.
- [11] C. Sorensen, D. Teal, "Health management for avionics performance," *Digital Avionics Systems*, vol. 1, pp. 3B3/1-3B3/5, Oct 2001.
- [12] E. J. Lundquist, J. R. Nagel, S. Wu, B. Jones, and C. Furse, "Advanced Forward Methods for Complex Wire Fault Modeling," *Sensors Journal, IEEE*, vol. 13, no. 4, pp. 1172-1179, April 2013.
- [13] S. Wu, C. Lo, and C. Furse, "Noncontact Probes for Wire Fault Location With Reflectometry," *Sensors Journal, IEEE*, vol. 6, no. 6, pp. 1716-1721, 2006.

- [14] D. M. Pozer, *Microwave Engineering*. Hoboken, NJ: John Wiley & Sons, 2005.
- [15] J. G. Proakis, *Digital Communications*, 4th ed. New York: McGraw-Hill, 2001.
- [16] C. R. Paul, *Analysis of Multiconductor Transmission Lines*. Hoboken: John Wiley & Sons, 2008.
- [17] J. R. Nagel, "Introduction to the Finite-Difference Time-Domain (FDTD) Algorithm".
- [18] H. A. Bethe, "Theory of diffraction by small holes," *The Physical Review*, vol. 66, no. 7-8, pp. 163-182, Oct 1944.
- [19] E. L. Ginzton and P. S. Goodwin, "A Note on Coaxial Bethe-Hole Directional Couplers," *Proceedings of the IRE*, vol. 38, no. 3, pp. 305-309, March 1950.
- [20] T. Scholz, "Impedance of Rectangular Slots in a Round Coaxial Tube," Berlin, Germany,.
- [21] Z. Jianhua, C. Xiuqiao, and J. Peng, "Coupling effects of high power microwave," in *Computational Electromagnetics and Its Applications*, Nov. 2004.
- [22] F. T. Ulaby, E. Michielssen, and U. Ravaioli, "Transmission Lines," in *Fundamentals of Applied Electromagnetics*. Upper Saddle River, NJ: Pearson Education, 2010.
- [23] C. Furse, B. Jones, and L. Thomson, "Non-Contact Connections for Reflectometry," in *Aircraft Airworthiness & Sustainment*, Baltimore, 2012.
- [24] M. Schamberger, S. Kosanovich, and R. Mittra, "Parameter Extraction and Correction for Transmission Lines and Discontinuities Using the Finite-Difference Time-Domain Method," *IEEE Transactions on Microwave Theory and Techniques*, vol. 44, no. 6, June 1996.
- [25] C. Liu, A. P. Hu, and M. Budhia, "A generalized coupling model for Capacitive Power Transfer systems," in *IECON 2010 - 36th Annual Conference*, Nov. 2010.
- [26] Y. Ogashara, M. Hashimoto, and T. Onoye, "Measurement analysis of inductive coupling noise in 90nm global interconnects," *IEEE Journal of Solid-State Circuits*, vol. 43, no. 3, pp. 718-728, March 2008.
- [27] E. C. Snelling, *Soft Ferrites Properties and Applications.*: Butterworth & Co., 1998.
- [28] Inc. Ceramic Magnetics. (2012) [Online]. <http://www.cmiferrite>.
- [29] J. R. Nagel, Solving the generalized poisson equation using the finite-difference method (FDM), January 2011, Feature Article, IEEE APS Homepage.